UNIVERSIDADE FEDERAL DE SÃO CARLOS
CENTRO DE CIÊNCIAS EXATAS E DE TECNOLOGIA
DEPARTAMENTO DE QUÍMICA
PROGRAMA DE PÓS-GRADUAÇÃO EM QUÍMICA

SÍNTESE E CARACTERIZAÇÃO DE VANADATOS DE PRATA E FORMAÇÃO DE NANOPARTÍCULAS DE PRATA POR ELETRO-IRRADIAÇÃO

Regiane Cristina de Oliveira*

Tese apresentada como parte dos requisitos para obtenção do título de DOUTORA EM CIÊNCIAS, área de concentração: FÍSICO-QUÍMICA.

Orientador: Elson Longo

*** CAPES**

São Carlos - SP
2018

UNIVERSIDADE FEDERAL DE SÃO CARLOS

Centro de Ciências Exatas e de Tecnologia
Programa de Pós-Graduação em Química

Folha de Aprovação

Assinaturas dos membros da comissão examinadora que avaliou e aprovou a Defesa de Tese de Doutorado da candidata Regiane Cristina de Oliveira, realizada em 19/02/2018:

Prof. Dr. Elson Longo da Silva
UFSCar

Prof. Dr. Elton Fabiano Sitta
UFSCar

Prof. Dr. Máximo Siu Li
IFSC/USP

Prof. Dr. Mario Cilense
UNESP

Prof. Dr. Luiz Fernando Gorup
UFSCar

AGRADECIMENTOS

Agradeço a Deus por toda bondade e misericórdia nesta etapa;

Ao Professor Dr. Elson Longo, pela orientação neste trabalho, aos ensinamentos e oportunidades a mim concedida.

Aos Prof. Dr. Juan Andrés e Profª. Dra. Lourdes Gracia pelos ensinamentos e contribuição aos trabalhos produzidos.

Ao IFSC, principalmente ao Prof. Dr. Máximo Siu Li pelas medidas de fotoluminescência e contribuição aos trabalhos realizados.

A todos do laboratório LIEC-CDMF (UFSCar e UNESP-Araraquara), IQ-UNESP (Araraquara), FOAr-UNESP (Araraquara), professores, estudantes, técnicos e funcionários que me auxiliaram durante essa trajetória.

Ao programa de Pós-Graduação em Química da Universidade Federal de São Carlos.

À minha família por todo sustento e carinho durante esta trajetória.

Aos meus amigos por toda convivência e incentivo.

A CAPES pela bolsa concedida.

PUBLICATIONS

Present Publications:

1. "Disclosing the Electronic Structure and Optical Properties of $Ag_4V_2O_7$ crystals: Experimental and Theoretical Insights" Oliveira, R. C.; Gracia, L.; Assis, M.; Li, M. S.; Andres, J.; Longo, E.; Cavalcante, L. S. CrystEngComm (Cambridge. Online), 18, 6483-6491 DOI: 10.1039/C6CE01269H (2016).

2. "Effect of metallic Ag growth on the electrical resistance of 3D flower-like $Ag_4V_2O_7$ crystals" Oliveira, R. C.; Zanetti, S. M.; Assis, M.; Penha, M.; Mondego, M.; Cilese, M.; Longo, E.; Cavalcante, L. S. Journal of the American Ceramic Society, 100, 2358-2362 DOI: 10.1111/jace.14803 (2017).

Other Publications:

3. "Mechanism of Antibacterial Activity via Morphology Change of α-$AgVO_3$: Theoretical and Experimental Insights" Oliveira, R. C.; Foggi, C. C.; Teixeira, M. M.; Silva, M. D. P.; Assis, M.; Francisco, E. M.; Pimentel, B. N. A. S.; Perreira, P. F.; Vergani, C. E.; Machado, A. L.; Andrés, J.; Gracia, L.; Longo, E. ACS Applied Materials & Interfaces, 9, 11472–11481 DOI: 10.1021/acsami.7b00920 (2017).

4. "An Experimental and Computational Study of β-$AgVO_3$: Optical Properties and Formation of Ag Nanoparticles" Oliveira, R. C.; Assis, M.; Teixeira, M. M.; Silva, M. D. P.; Li, M. S.; Andres, J.; Gracia, L.; Longo, E. Journal of Physical Chemistry. C, 120, 12254–12264 DOI: 10.1021/acs.jpcc.6b02840 (2016).

5. "Blue and red light photoluminescence emission at room temperature from $CaTiO_3$ decorated with α-Ag_2WO_4" Mondego, M.; Oliveira, R. C.; Penha, M.; Li, M. S.; Longo, E. Ceramics International, 43, 5759-5766 DOI: 10.1016/j.ceramint.2017.01.121.

6. "Tuning the morphology, optical and antimicrobial properties of α-Ag_2WO_4 microcrystals by using different solvents" Foggi, C. C.; Oliveira, R. C.; Fabbro, M. T.; Vergani, C.; Andrés, J.; Longo, E.; Machado, A. Crystal Growth & Design, 17, 6239–6246 DOI: 10.1021/acs.cgd.7b00786 (2017).

7. "$ZnWO_4$ nanocrystals: Synthesis, morphology, and photoluminescence and photocatalytic properties" Pereira, P. F. S.; Gouveia, A. F.; Assis, M.; Oliveira, R. C.; Pinatti, Ivo. M.; Penha, M.; Gonçalves, R. F.; Gracia, L.; Andrés, J.; Longo. E. Physical Chemistry Chemical Physics, DOI: 10.1039/C7CP07354B (2017).

8. "Towards the scale-up of the formation of nanoparticles on α-Ag_2WO_4 with bactericidal properties by femtosecond laser irradiation" Assis, M.; Cordoncillo, Eloisa; Torres-Mendieta, R.; Beltrán-Mir, H.; Mínguez-Vega, G.; Oliveira, R.; Leite, E. R.; Foggi, C. C.; Vergani, C. E.; Longo, E.; Andres, J.; Scientific Reports, (2018)

9. "α and β-$AgVO_3$ polymorphs as photoluminescent materials: An example of temperature-driven synthesis" Oliveira, R. C.; Teixeira, M. M.; Costa, J. P.; Penha, M.; Francisco, E. M.; Li, M. M.; Longo, E.; Gracia, L.; Andrés, J. Ceramics International, (2018).

TABLES LIST

Disclosing the electronic structure and optical properties of $Ag_4V_2O_7$ crystals: experimental and theoretical insights

Effect of metallic Ag growth on the electrical resistance of 3D flower-like $Ag_4V_2O_7$ crystals

FIGURES LIST

Disclosing the electronic structure and optical properties of $Ag_4V_2O_7$ crystals: experimental and theoretical insights

Effect of metallic Ag growth on the electrical resistance of 3D flower-like $Ag_4V_2O_7$ crystals

RESUMO

Síntese e Caracterização de Vanadatos de Prata e Formação de Nanopartículas de Prata por Eletro-Irradiação. Devido as suas propriedades físico-químicas, bactericidas e fotocatalíticas, os Vanadatos de Prata têm atraído interesses científicos e tecnológicos. Este trabalho teve como objetivo sintetizar, via método de Co-Precipitação (CP), vanadato de prata, em especial o pirovanadato $Ag_4V_2O_7$. Os métodos de sínteses desse material propostos na literatura, exigem altas temperaturas, longos tempos de processamento e sofisticados equipamentos. Além disso, o produto final é obtido com tamanhos e morfologias não homogêneas e contendo fases deletérias. Neste sentido, o objetivo desse trabalho foi realizar uma otimização do método de CP, afim de obter o $Ag_4V_2O_7$ monofásico e com morfologia definida. Os materiais foram caracterizados por Difração de Raios-X (DRX), refinamento Rietveld, espectroscopia Raman (Raman), Ultravioleta-visível (UV-Vis) e Fotoluminescência (PL). As morfologias dos materiais foram estudadas por MEV (Microscopia Eletrônica de Varredura). Recentemente, o nosso grupo relatou, pela primeira vez, a nucleação e crescimento *in situ* de nanopartículas (NPs) de Ag sobre a superfície dos semicondutores de óxidos binários de prata, conduzido por um feixe de elétrons, acelerado sob alto vácuo (a partir de um microscópio eletrônico de transmissão/ varredura) e observaram que este fenômeno realça as propriedades desse material. Com esta motivação, neste trabalho foi realizado um estudo do crescimento de NPs de Ag sobre a superfície do $Ag_4V_2O_7$, o efeito do crescimento de NPs de Ag sobre as propriedades eletrônicas do material foram avaliados. Finalmente, cálculos teóricos de primeiros princípios, baseados na Teoria do Funcional da Densidade (DFT), foram utilizados na compreensão das observações experimentais.

ABSTRACT

Synthesis and Characterization of Silver Vanadates and Formation of Silver Nanoparticles by Electro-Irradiation. Due to its physico-chemical, bactericidal and photocatalytic properties, Silver vanadium oxides (SVOs) have attracted increasing attention due to their excellent physicochemical properties and diverse applications. The aim of this work was to synthesize, by Co-Precipitation (CP) method, SVOs in especial the $Ag_4V_2O_7$ pyrovanadate. The synthesis methods of this material proposed in the literature, require high temperatures, long processing times and sophisticated equipment. In addition, the final product is obtained with nonhomogeneous sizes and morphologies and containing deleterious phases. In this sense, the objective of this work was to perform an optimization of the CP method, in order to obtain the monophasic $Ag_4V_2O_7$ with defined morphology. The materials were characterized by X-ray Diffraction (XRD), Rietveld refinement, Raman, Ultraviolet-visible (UV-Vis) and Photoluminescence (PL) spectroscopy. The morphologies of the materials were studied by SEM (Scanning Electron Microscopy). Theoretical calculations of first principles, based on the Functional Density Theory (DFT), were used in the understanding of the experimental observations. Recently, our group reported, for the first time, nucleation and in situ growth of Ag nanoparticles (NPs) on the surface of semiconductors of silver binary oxides, conducted by an electron beam, accelerated under high vacuum (from an electron transmission/scanning microscope) and observed that this phenomenon highlights the properties of this material. Finally, a study of the growth of Ag NPs on the surface of $Ag_4V_2O_7$ was carried out, the effect of growth of Ag NPs on the electronic properties of the material were evaluated.

SUMMARY

1. GENERAL INTRODUCTION

Recently SVOs (Silver Vanadates Oxides), such as $AgVO_3$, $Ag_4V_2O_7$, Ag_3VO_4 have attracted a lot of interest due to their properties (antibacterial, optical, magnetic, high ionic conductivity, luminescence, catalytic activity and storage of energy) (Sellami, Melliti et al. 2009, Dai, Luo et al. 2010, Rajagopal, Nataraj et al. 2010, Lin, Jiexin et al. 2012, Muthamizh, Suresh et al. 2015, Xu, Cheng et al. 2015)

The redox behavior, the lamellar structure, and the structural characteristics, allow the SVOs to be transformed into different SVOs. The reaction conditions and material, stoichiometry, and the methodology applied in their synthesis determines the type of SVOs that will be obtained. This phenomenon can be attributed to the flexibility of their geometric structure, in which the Ag and V atoms can adopt different sites of coordination. The electronic properties of SVOs are associated with the valence bands hybridization of the 3d orbitals of V, 2p of O and 4d of Ag. This hybridization causes reduction on the band gap value and a high dispersion in the valence band (Ju, Fan et al. 2013, Oliveira, Assis et al. 2016, Oliveira, Gracia et al. 2016)

In particular, the silver vanadate $Ag_4V_2O_7$ has shown to be very promising due to its photocatalytic and photoelectrochemical properties. This material has an orthorhombic structure. The crystal, shown in Figure 3, is constructed of two types of clusters of Ag and V atoms: $[VO_4]$ and $[VO_5]$, in which the V atoms are coordinated by four and five O atoms, forming distorted clusters of tetrahedron and trigonal bipyramid, respectively. While the Ag atoms are coordinated at five and six O atoms forming clusters $[AgO_5]$ and $[AgO_6]$, respectively. The $[AgO_5]$ clusters form trigonal bipyramidal and square pyramidal distorted polyhedra, while the clusters of $[AgO_6]$ form octahedra and triangular prism. The crystalline solid consists of a network formed by (...$[VO_4]$-$[AgO_6]$-$[VO_5]$-$[AgO_5]$-$[VO_4]$…) interconnected and agglomerated (Oliveira, Gracia et al. 2016).

Several techniques, such as mechanical-chemical reactions, oxide mixing, solid-state reaction, precipitations with calcination over long periods of time, and molten metal fluxes have been reported in the synthesis of these materials. However, these methods require high temperatures, long processing times, and sophisticated equipment that involves high maintenance costs (Konta, Kato et al. 2003, Hu, Hu et al. 2008, Huang, Pan et al. 2009, Chen, Pan et al. 2010, Dai, Luo et al. 2010, Huang, Cheng et al. 2010, Chang, Li et al. 2011, Belver, Adán et al. 2013, Ran, McEvoy et al. 2016). Moreover, in these cases, the final product is obtained with nonhomogeneous sizes and morphologies and

some deleterious phases, such as V_2O_5 and Ag_2O, which make many types of applications unfeasible.

To avoid these disadvantages, several synthetic routes have been recently developed. In particular, our laboratory has been synthesize various binary metal oxides, including Ag_2WO_4, Ag_2MoO_4 and Ag_3PO_4, using the CP technique, which has the following characteristics: good reproducibility, low processing temperatures and environmentally friendly solvents (water/ethanol/acetone). This method corresponds to the preparation of homogeneous solutions containing the desired ions and the stoichiometric precipitation of this multicomponent system in the form of hydroxides, oxides, oxalates, among others. In this technique, it is possible to obtain semiconductor solids with defined morphology, homogeneous and stoichiometric (Kakihana 1996).

The basic principle of the CP method is dissolve the precursor reactants separately in a solution. Then the ionic species formed are mixed and precipitated, to give rise the material of interest. Thereafter, the powder obtained must be washed to remove the viewer ions, and dried in an oven (Segal 1997). Since this technique is based on the solubility constant between the precipitant phases, it is critical that all the metal ions precipitate simultaneously to obtain a homogeneous product. In addition, precise control over the temperature, the pH of the solution and the concentration of the reactants is required (Segal 1997).

Unlike the $Ag_4V_2O_7$ synthesis methods already published in the literature, in the CP method, by modifying the synthesis parameters, it is possible to control the morphology of the materials. According to the literature, the morphology of semiconductor materials plays an important role in the final properties of the semiconductor, as well as the chemical composition, crystalline structure or even the crystal size (Moreira, Mambrini et al. 2008). This occurs essentially due to the excess of energy accumulated at the interfaces of the particles isolated, which are regions with great density of unsaturations (oxygen vacancies). This feature highlights the importance of research related to the surfaces and morphologies of materials with potential technological applications, as it allows the preparation of a range of materials with unique properties (Geoffrey A Ozin 2008). Thus, it is necessary to control the morphology of the semiconductor crystal.

Recently, our group reported, for the first time, the in situ nucleation and growth of Ag NPs on the surface of some silver compounds, such as Ag_2WO_4, Ag_2MoO_4 and Ag_3PO_4, driven by an accelerated electron beam under high vacuum (from an electronic microscope) (Longo, Cavalcante et al. 2013, Longo, De Foggi et al. 2014), (Longo, Avansi

et al. 2016), (Fabbro, Saliby et al. 2016) (Botelho, Sczancoski et al. 2015). This phenomenon generates new possibilities of applications, as well as, photocatalyst, sensor and bactericide (Longo, Cavalcante et al. 2013, Longo, De Foggi et al. 2014, S., Andres et al. 2015, Fabbro, Gracia et al. 2016, Fabbro, Saliby et al. 2016, Longo, Avansi et al. 2016, Oliveira, Assis et al. 2016, Silva, Goncalves et al. 2016).

The discovery occurred when scientists were studying the properties of α-Ag_2WO_4 crystals in a MET, and observed the formation of protuberances on the surface of the semiconductor after the crystals were subjected to electro-irradiation. By repeating the experiment and characterizing the samples using an EDS (X-ray Dispersive Energy Spectroscopy), it was concluded that these protuberances were Ag NPs, generated from the silver tungstate matrix. Due to this result, our group is dedicated a research project related to the study of the nucleation processes and growth, in real time and in situ, of Ag NPs by accelerated electron beam irradiation from an electron microscope (MET / SEM) under high vacuum, in different silver semiconductors.

In 2013, for the first time, Longo et al (Longo, Cavalcante et al. 2013), reported the real-time in situ nucleation and growth of Ag filaments on α-Ag_2WO_4 crystals driven by an accelerated electron beam from an electronic microscope under high vacuum. By using experimental techniques combined with first-principles modelling based on density functional theory, a mechanism for the Ag filament formation followed by a subsequent growth process from the nano- to micro-scale was proposed: irradiated electrons are absorbed by the external and higher charged tetrahedral [AgO_4] clusters, followed by a subsequent disproportionation reaction with the angular [AgO_2] clusters. This procedure produces [AgO_6] clusters and metallic Ag that migrate to the surface, resulting in the local amorphisation of α-Ag_2WO_4 (Longo, Cavalcante et al. 2013).

Roca et al, reported for first time the in situ formation, growth, and subsequent reabsorption of Ag nanoparticles on the surface of this metastable β-Ag_2WO_4, which was induced by electron beam irradiation under high vacuum. Energy dispersive spectroscopy (EDS) confirmed that Ag NPs grew on the β-Ag_2WO_4 surface. The researchers noted that nucleation, growth and complete reabsorption of Ag NPs was faster than the similar processes observed for α-Ag_2WO_4. A higher organization in the β-Ag_2WO_4 hexagonal structure is assumed, in comparison with the α-Ag_2WO_4 orthorhombic structure, then it is possible to explain the faster nucleation and absorption of Ag NPs in β-Ag_2WO_4 (Alvarez Roca, Lemos et al. 2016).

In 2015, theoretical and experimental studies were realized on the structure, optical properties, and growth of silver nanostructures in silver phosphate (Ag_3PO_4) by Botelho et al (Botelho, Sczancoski et al. 2015). First-principles calculations, within a quantum theory of atoms in molecules framework, have been carried out to understanding of the observed nucleation and early evolution of Ag nanoparticles on Ag_3PO_4 crystals, driven by an accelerated electron beam from an electronic microscope under high vacuum. The authors concluded that when up to five electrons were taken into account in the theoretical calculations, a pronounced modification in the Ag−O bond lengths of [AgO_4] clusters was detected, suggesting that the incorporation of electrons induces the growth of Ag in the microparticles (Botelho, Sczancoski et al. 2015).

A combined experimental and theoretical study is realized by Andrés et al (Andres et al. 2015) to understand the nucleation and early evolution of Ag filaments on β-Ag_2MoO_4 crystals, driven by an accelerated electron beam from an electronic microscope under high vacuum. The researchers concluded that the Ag nucleation and formation on β-Ag_2MoO_4 are a result of structural and electronic changes of the AgO_4 tetrahedral cluster as a constituent building block of β-Ag_2MoO_4, consistent with Ag metallic formation (Andres et al. 2015).

Using FE-SEM and TEM micrographs, Fabrro et al (Fabrro, Gracia et al. 2016 revealed the morphology and the growth of Ag nanoparticles on Ag_2CrO_4 microcrystals during electron beam irradiation. These events were directly monitored in real-time. Theoretical analyses based on the density functional theory level indicate that the incorporation of electrons is responsible for structural modifications and formation of defects on the [AgO_6] and [AgO_4] clusters, generating ideal conditions for the growth of Ag nanoparticles (Fabbro, Gracia et al. 2016).

Therefore, it is believed that when the semiconductor receives the electron irradiation, the various clusters that constitute the crystals are disorganized and reorganized, occurring electron transfers by means of oxidation/reduction reactions, from these reactions occurs the formation of Ag NPs. However a more detailed study of this phenomenon is necessary. (Longo, Cavalcante et al. 2013, Longo, De Foggi et al. 2014, Botelho, Sczancoski et al. 2015, S., Andres et al. 2015, Fabbro, Gracia et al. 2016, Fabbro, Saliby et al. 2016, Longo, Avansi et al. 2016, Silva, Goncalves et al. 2016)

Modifications of the semiconductors properties by Ag NPs are of particular interest because of their excellent performance and wide range of applications in solar cells,

bactericide, chemical sensing, and photocatalysis (Linic, Christopher et al. 2011, Yu, Wei et al. 2013, Luo, Liu et al. 2014).

Experimental studies have reported that the Ag NPs deposition (with excellent electronic conductivity and strong ability to trap electrons) on the surfaces of SVOs has improved their electronic properties, since the formation of heterojunction increase the separation rate of the pair electron-hole (Linic, Christopher et al. 2011, Yu, Wei et al. 2013, Luo, Liu et al. 2014). In addition, the growth of Ag NPs on the surface of the semiconductor creates defects in the crystalline lattice this can significantly alter the electronic properties of the material, creating a more or less resistant material.

In this context, the aim of this study was investigate the optical and electronic properties of $Ag_4V_2O_7$ semiconductor prepared by the CP method. To the best of our knowledge, the preparation of $Ag_4V_2O_7$ by this method has not been reported so far. Further, these experimental results were supported by theoretical calculations. The study of the Ag NPs growth on the $Ag_4V_2O_7$ surface by accelerated electron beam irradiation from an electron microscope (MET/MEV) under high vacuum will be carried out. And a study of the electrical resistance changes with the growth of metallic Ag NPs in the surface will be realized.

2. PUBLISHED ARTICLES

2.1. Disclosing the electronic structure and optical properties of $Ag_4V_2O_7$ crystals: experimental and theoretical insights

Abstract

This work combines experimental and computational techniques to exploit the best of both methodologies and thus provide a tool for understanding the geometry, cluster coordination, electronic structure, and optical properties of $Ag_4V_2O_7$ crystals. This tool has been developed to create structural models and enable a much more complete and rapid refinement of 3D (three dimensional) structures from limited data, aiding the determination of structure–property relationships and providing critical input for materials simulations. $Ag_4V_2O_7$ crystals were synthesized by a simple precipitation method from an aqueous solution at 30 °C for 10 min. The obtained crystals were characterized by X-ray diffraction (XRD) and Rietveld refinement, and micro-Raman spectroscopy. The crystal

morphology was determined by field emission scanning electron microscopy (FESEM), and the optical properties were investigated by ultraviolet-visible (UV-Vis) diffuse reflectance spectroscopy and photoluminescence (PL) measurements. The geometric and electronic structures of $Ag_4V_2O_7$ crystals were investigated by first-principles quantum-mechanical calculations based on the density functional theory. The theoretical results agree with the experimental data to confirm that $Ag_4V_2O_7$ crystals have an orthorhombic structure, and that the building blocks of the lattice comprise two types of V clusters, $[VO_4]$ and $[VO_5]$, and two types of Ag clusters, $[AgO_5]$ and $[AgO_6]$. This type of fundamental studies, which combine multiple experimental methods and first-principles calculations, have been proved valuable in obtaining a basic understanding of the local structure, bonding, band gap, and electronic and optical properties of $Ag_4V_2O_7$ crystals.

1. Introduction

In recent years, silver vanadates ($AgVO_3$, $Ag_2V_4O_{11}$, Ag_3VO_4, $Ag_4V_2O_7$, etc.) have attracted increasing attention due to their widespread potential applications resulting from their special optical, electronic, and chemical properties.[1–18] The excellent properties of silver vanadates can be attributed to the flexibility of their geometric structure, in which Ag and V ions can adopt different local coordinations, as well as the electronic properties associated with the hybridization of the valence bands of the V 3d, O 2p, and Ag 4d orbitals, yielding a narrow band gap and highly dispersed valence bands.[19–21]

Among the reported silver vanadates, silver pyrovanadate ($Ag_4V_2O_7$) has drawn extensive interest in the field of photocatalysis.[6,7,10] Various techniques, such as mechanochemical reactions,[22] oxide mixture or solid-state reaction,[2] precipitation with calcination at long periods of time,[2] and molten metal fluxes[23] have been reported. However, these methods require high temperatures, long processing times, and sophisticated equipment with high maintenance costs. In addition, the final product is obtained with some deleterious phases, such as V_2O_5, amorphous $AgVO_3$, Ag_3VO_4, and Ag_2O, with inhomogeneous sizes and shapes. To avoid these draw-backs, several synthetic routes have recently been developed and employed in the preparation of $Ag_4V_2O_7$ micro and nanocrystals,[10,24] and pure $Ag_4V_2O_7$ crystals have been obtained through several wet chemistry-based techniques, such as conventional and surfactant-assisted hydrothermal syntheses[5,7,9,25] or microemulsions.[26] These methods circumvent the problems encountered in earlier synthetic methods and facilitate the synthesis of single phase crystals with homogeneous sizes and shapes. In particular, our lab has

successfully achieved the preparation of various complex ternary metal oxides, including α-Ag_2WO_4 [27] and β-Ag_2WO_4 [28] using facile and readily scalable techniques in environmentally friendly solvents (water) at low processing temperatures.

To the best of our knowledge, the geometric and electronic structures of $Ag_4V_2O_7$ crystals have not been investigated either theoretically or experimentally. This encouraged us to investigate the geometry, cluster coordination, and electronic structure of $Ag_4V_2O_7$ microcrystals. Five years ago, our research groups initiated a major experimental and theoretical collaboration to elucidate the structure, chemical bonding, and electronic and optical properties of numerous ternary metal oxide photocatalysts, bactericides, sensors, photoluminescent complexes, etc., such as α-Ag_2WO_4,[27,29–32], β-Ag_2WO [28], β-Ag_2 MoO_4 [33] and Ag_3PO_4. [34,35] These studies have made significant advances in the formal understanding of the properties and application of these compounds at a qualitative or semiquantitative level, by combining experimental data and first-principles calculations.

Here, we report for the first time the synthesis of $Ag_4V_2O_7$ microcrystals by a simple precipitation method (PM) at low temperature. The synthesized $Ag_4V_2O_7$ crystals were characterized by X-ray diffraction (XRD) and Rietveld refinement, Raman spectroscopy, field emission scanning electron microscopy (FE-SEM), ultraviolet-visible (UV-Vis) diffuse reflectance spectroscopy, and photoluminescence (PL) measurements. First-principles quantum-mechanical calculations using the density functional theory (DFT) were carried out in order to correlate the results of XRD, Raman spectroscopy, FE-SEM, and the PL measurements for $Ag_4V_2O_7$. There is a need to link the length and complexity scales between the levels of theory used in calculations and the variable space in which experiments take place; the present work can thus be considered as an attempt to bridge this gap.

2. Experimental and theoretical methods

2.1. Experimental details

The precursors utilized in this synthesis were silver nitrate ($AgNO_3$) (99.0% purity, Synth) and ammonium monovanadate (NH_4VO_3) (99% purity, Aldrich). Initially, 1×10^{-3} mol NH_4VO_3 were dissolved in 60 mL of distilled water at 30 °C, under magnetic stirring for 15 minutes. Then, 1×10^{-3} mol $AgNO_3$ were dissolved in 15 mL of distilled water, under magnetic stirring for 15 minutes; to this solution, a few drops of ammonium hydroxide (NH_4OH) (30% in NH_3, Synth) were added until the solution became clear. Both solutions

were quickly mixed, promoting the instantaneous formation of solid $Ag_4V_2O_7$ precipitates (orange coloration). To accompany the change of morphologies, the PM was performed at 30 °C for 10 min. The precipitate was centrifuged, washed with distilled water several times, and dried in a conventional furnace at 60 °C for some hours.

2.2. Characterization

X-ray diffraction was carried out using a Rigaku-DMax/ 2500PC (Japan) with Cu Kα radiation (λ = 1.5406 Å) in the 2θ range from 10° to 110° with a scanning rate of 0.02° min^{-1}. Micro-Raman spectroscopy was carried out using a T64000 spectrometer (Horiba Jobin-Yvon, Japan) coupled to a CCD Synapse detector and an argonion laser, operating at 514 nm with a maximum power of 7 mW. The spectra were measured in the range from 100 cm^{-1} to 1000 cm^{-1}. UV-vis spectra were obtained using a Varian spectrophotometer (model: Cary 5G, USA) in diffuse reflection mode. The morphologies were investigated using a field emission scanning electron microscope (FE-SEM) (Supra 35-VP, Carl Zeiss, Germany) operated at 15 KV. The PL measurements were performed using a Monospec 27 monochromator (Thermal Jarrel Ash, USA) coupled to an R446 photomultiplier (Hamamatsu Photonics, Japan). A krypton ion laser (Coherent Innova 90K, USA) (λ = 350 nm) was used as an excitation source, keeping its maximum output power at 500 mW. After passing through the optical chopper, the maximum laser power was reduced and kept at 40 mW on the samples. An optical parametric oscillator was employed for lifetime measurements. All experimental measurements were performed at room temperature.

2.3. Theoretical calculations

Calculations on the periodic $Ag_4V_2O_7$ structure were performed using the CRYSTAL14 software package.[36] Tungsten was described by a large-core ECP, derived by Hay and Wadt, and modified by Cora et al.[37] Silver and oxygen centers were described using HAYWSC-311d31G and O (6-31d1G) basis sets, respectively, which were obtained from the Crystal website.[38] For the range separated hybrid functional, screened Coulomb HSE06 was used in order to obtain the accurate band gaps for the computed structures. The diagonalization of the Fock matrix was performed at adequate k-point grids in the reciprocal space. The thresholds controlling the accuracy of the calculation of the Coulomb and exchange integrals were set to 10^{-8} and 10^{-14}, respectively, and the percentage of Fock/Kohn–Sham matrix mixing was set to 40 (IPMIX keyword).[36] The

empirical correction scheme to energy that considers the long-range dispersion contributions proposed by Grimme39 and implemented by Bucko et al.[40] for periodic systems was used. In the relaxed configuration, the forces on the atoms are less than 0.0001 hartree per bohr = 0.005 eV $Å^{-1}$, and deviations of the stress tensor from a diagonal hydrostatic form are less than 0.1 GPa. The band structure and the density of states (DOS) projected on atoms and orbitals of bulk $Ag_4V_2O_7$ were constructed along the appropriate high-symmetry directions of the corresponding irreducible Brillouin zone. The vibrational frequency calculation in CRYSTAL14 is performed at the Γ-point within the harmonic approximation, and the dynamic matrix is computed by the numerical evaluation of the first derivative of analytical atomic gradients.

First-principles total energy calculations on the periodic $Ag_4V_2O_7$ structure were performed within the density functional theory (DFT) along with projector augmented wave (PAW) potentials implemented in the VASP program.[41] The Kohn–Sham equations were solved using the screened hybrid functional proposed by Heyd, Scuseria, and Ernzerhof (HSE),[42] in which a percentage of the exact nonlocal Fock exchange was added to the Perdew, Purke, and Ernzerhof functional (25%), with a screening of 0.2 $Bohr^{-1}$ applied to the partition of the Coulomb potential into long-range and short-range terms. The plane-wave expansion was truncated at a cut-off energy of 400 eV and the Brillouin zones were sampled using Monkhorst–Pack special k-point grids to ensure geometrical and energetic convergence. Conjugate gradient algorithms were used for unit-cell relaxations and atomic positions, until the residual forces and stress in the equilibrium geometry were of the order of 0.005 eV $Å^{-1}$ and 0.01 GPa, respectively. The band structure and the density of states (DOS) projected on the atoms and orbitals of bulk $Ag_4V_2O_7$ were constructed along the appropriate high-symmetry directions of the corresponding irreducible Brillouin zone. Vibrational-frequency calculations were performed at the Γ-point within the harmonic approximation, and the dynamic matrix was computed by numerical evaluation of the first derivative of the analytical atomic gradients. Therefore, the DFT method has proven to be one of the most accurate methods for the computation of the electronic structure of solids.[43–48]

3. Results and discussion

3.1. XRD pattern and Rietveld refinement analysis

Fig. 1(a) and (b) show the XRD pattern and Rietveld refinement plot of the $Ag_4V_2O_7$ microcrystals, respectively. $Ag_4V_2O_7$ was first characterized by Masse et al.[23] and Fig.

1(a) shows the XRD pattern corresponding to the orthorhombic structure, in agreement with the corresponding Inorganic Crystal Structure Database (ICSD) Card No. 38065 for the pure $Ag_4V_2O_7$ phase.[23] According to the literature,[23] pure $Ag_4V_2O_7$ microcrystals present a space group (Pbca), a point-group symmetry (D15), and sixteen molecular formula units per unit cell (Z = 16). In order to confirm this result, a structural refinement by means of the Rietveld method,[49] based on the construction of diffraction patterns calculated according to a structural model,[50] was performed using the general structure analysis (GSAS) program.[51]

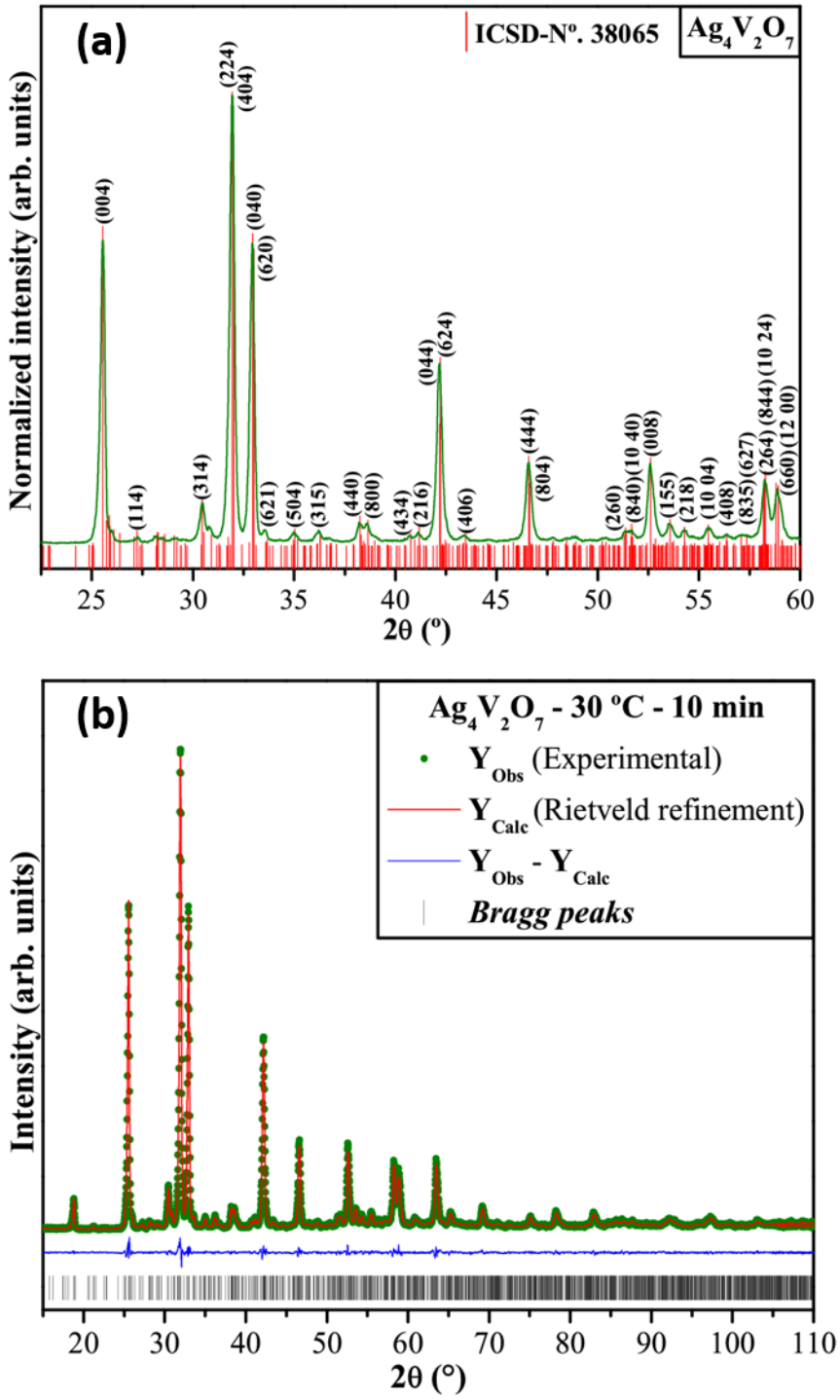

Fig. 1 (a) XRD pattern of 3D hexagon-like $Ag_4V_2O_7$ microcrystals obtained at 30 °C for 10 min and (b) Rietveld refinement plot of 3D hexagon-like $Ag_4V_2O_7$ microcrystals, respectively. The vertical lines in black colour indicate the position and relative intensity of the Inorganic Crystal Structure Database (ICSD) Card No. 38065 for the $Ag_4V_2O_7$ phase, respectively.

The calculated patterns were adjusted to fit the observed patterns and thus provide the structural parameters of the material and the diffraction profile. In this work, the Rietveld method was applied to adjust the atomic positions, lattice parameters, and unit cell volume. Fig. 1(b) shows that the structural refinement results are mostly consistent with the ICSD No. 38065 reported by Masse et al.[23] However, the low-angle region, where the most intense peaks are located, reveals a major difference related to narrow peaks and high intensities in the pattern.

The quality of a structural refinement is generally examined using R-values (R_{wp}, R_{Bragg}, R_p, χ^2, and S). These values were determined for our crystals and found to be consistent with an orthorhombic structure. However, the experimentally observed XRD patterns and theoretically calculated data display small differences near zero on the intensity scale, as illustrated by the line Y_{Obs}–Y_{Calc}. More details regarding the Rietveld refinement results are displayed in Table S1.† The Rietveld refinement plot for the $Ag_4V_2O_7$ microcrystals is shown in Fig. 1(b).

3.2. Unit cell representation, symmetry, geometry, and coordination of the clusters in $Ag_4V_2O_7$ crystals

Fig. 2(a) and (b) show a schematic representation of the orthorhombic $Ag_4V_2O_7$ unit cell in which different clusters, i.e. the local coordination of V and Ag atoms, are depicted. The symmetry, geometry, and coordination data for each cluster, as well as the lattice parameters and atomic positions calculated by geometry optimization, are listed, while those obtained from the Rietveld refinement data are presented in Table S1.†

The unit cell shown in Fig. 2(a) and (b) was modeled through the Visualization System for Electronic and Structural Analysis (VESTA) program (version 3.3.8 for Windows 7 64-bit).[52,53] Analysis of the results indicated that two types of clusters are the main building blocks of the structure for both V and Ag atoms: $[VO_4]$ and $[VO_5]$, in which V atoms are coordinated to four and five O atoms, respectively, and $[AgO_5]$ and $[AgO_6]$, in which Ag atoms are linked to five and six O atoms, respectively. The different types of local coordination for the Ag and V atoms, together with the Ag–O and V–O bond lengths corresponding to the minima, D_{min}, and maxima, D_{max}, are listed in Fig. 2(a). Analysis of the results revealed that $[VO_4]$ and $[VO_5]$ clusters are distorted tetrahedral and distorted trigonal bipyramidal polyhedral clusters, respectively. V_1 and V_4 (Fig. 2(a)) form distorted trigonal bypiramidal $[VO_5]$ clusters, while V_2 and V_3 form tetrahedral $[VO_4]$ clusters. Atoms Ag_1 and Ag_7, as well as Ag_8, are coordinated to five O atoms, forming distorted square-

based pyramidal and distorted trigonal [AgO_5] clusters, respectively; while Ag_2, Ag_3, Ag_5, and Ag_6 are bonded to six O atoms, which form distorted octahedral [AgO_6] clusters; and Ag_4 is at the center of a distorted triangular prism [AgO_6].

The lattice parameters, unit-cell volume, and internal atomic coordinates for $Ag_4V_2O_7$ from the Rietveld refinement and DFT calculations are reported in Tables S1(a) and (b) (ESI†), respectively. Analysis and comparison of both theoretical and experimental results show variations in the atomic positions of O atoms, which are associated with the fact that these atoms do not occupy fixed positions in the orthorhombic structure. Large variations in the position of O atoms in the lattice are also found in the structure. These findings explain why assignment of the atomic positions of O atoms is difficult, since subtle atomic rearrangements occur.

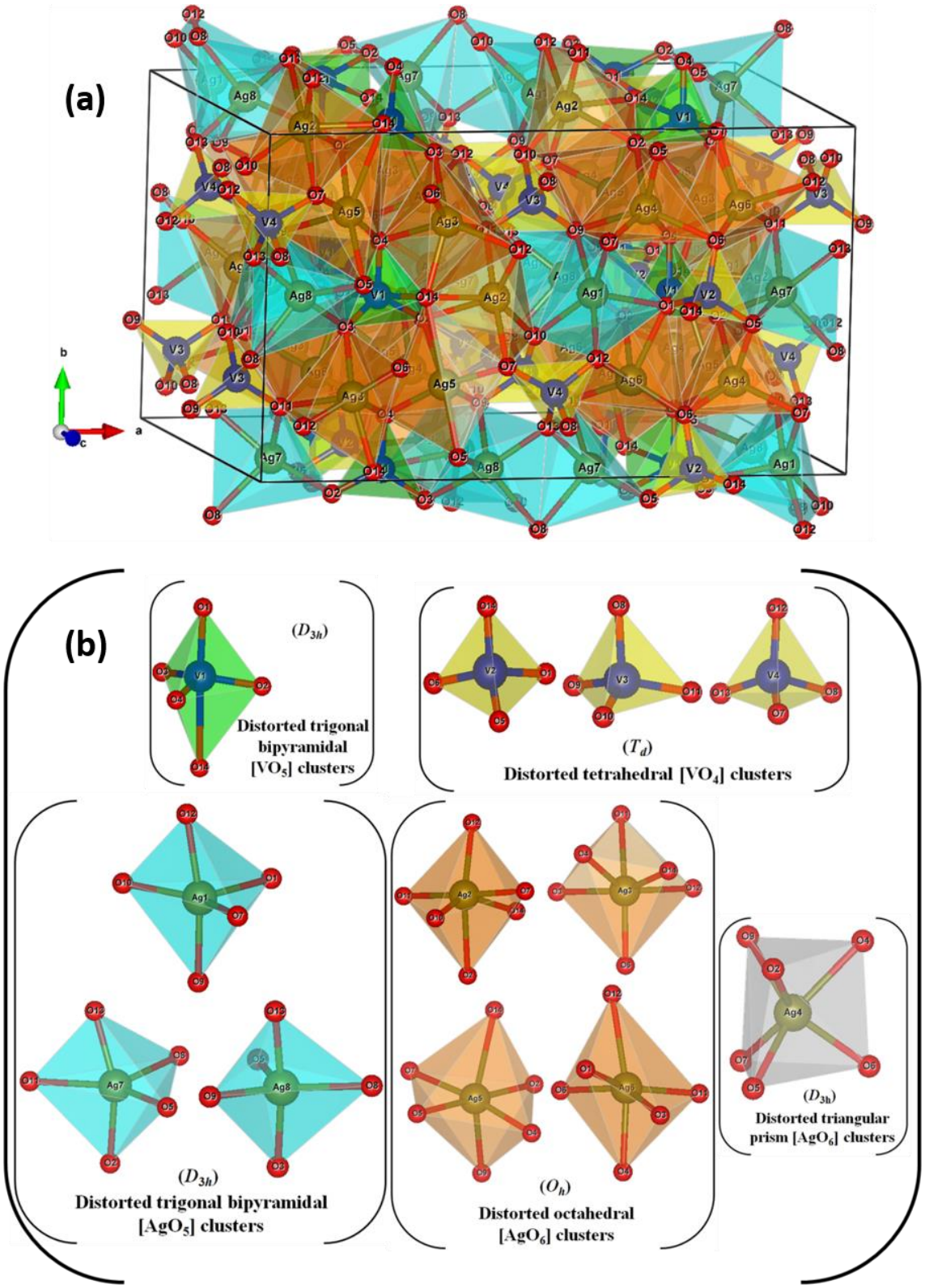

Fig. 2 Schematic representation of the (a) orthorhombic unit cells corresponding to pure $Ag_4V_2O_7$ crystals and (b) their clusters, respectively.

In order to interpret these data, we presume that these disagreements in the atomic positions of O atoms are attributed to the nature of the starting sample (polycrystalline powder or single crystal). Although single-crystal data are essential for the refinement of

crystal-structure models, we believe that the formation of different distortions in the cluster coordination, [AgO_y] (y = 5 and 6) and [VO_z] (z = 4 and 5), can lead to the formation of different types of distortions in the Ag–O and/or V–O bonds, as well as the O–Ag–O and/or O–V–O bond angles. This is due to the fact that cluster rotation influences the Ag–O and V–O bond lengths, as well as the Ag–O–Ag and V–O–V bond angles, due to the shift of the oxygen ions from the edge of the ideal structures. Therefore, the differences in both Ag–O and V–O bond lengths and O–Ag–O and O–V–O bond angles result in intrinsic structural order–disorder in this type of lattice, and $Ag_4V_2O_7$ crystals thus present different levels of distortion in their crystalline lattice due to the variety of coordination polyhedra. Subsequently, the positions of O, V, and Ag atoms are variable. A similar phenomenon has been previously reported for the α-Ag_2WO_4 [54] and β-Ag_2WO_4 phases.[28] XRD experiments provide only average structures.

A better understanding of the properties of this material requires more detailed information on local structures and cell parameters. In other words, if there is partial order in the distribution of Ag and V atoms, crystal cells observed at the local level should be different from those determined by XRD measurements. Raman spectroscopy probes the full vibrational spectrum of interest since it is sensitive to short-range structural order, i.e., the local coordination at both Ag and V centers.

3.3. Micro-Raman spectroscopy analysis

Raman spectroscopy can be employed as a probe to investigate the degree of structural order–disorder in materials at short-range: in our case, the local coordination of both Ag and V atoms associated with different clusters, [AgO_y] (y = 5 and 6) and [VO_z] (z = 4 and 5), as the building blocks of $Ag_4V_2O_7$ crystals. To the best of our knowledge, the Raman characteristics of $Ag_4V_2O_7$ have not been previously reported, either theoretically or experimentally. Consequently, we extended our systematic structural investigation toward Raman spectroscopy and the theoretical analysis of the vibrational modes of $Ag_4V_2O_7$. The micro-Raman spectrum of $Ag_4V_2O_7$ microcrystals is shown in Fig. 3.

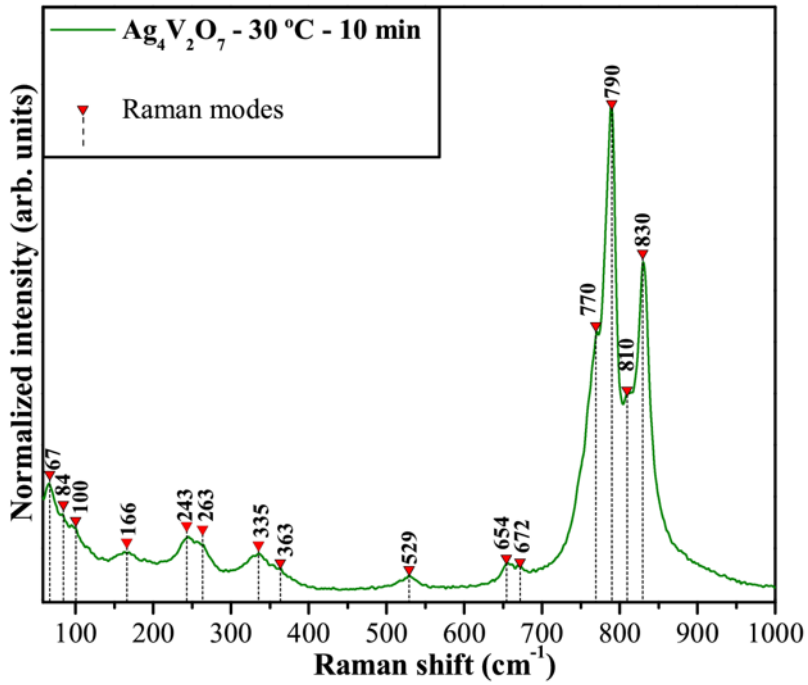

Fig. 3 Micro-Raman spectrum of 3D hexagon-like $Ag_4V_2O_7$ microcrystals and comparison between the relative positions of the theoretical and experimental Raman-active modes, respectively.

The micro-Raman spectrum revealed the presence of only fifteen Raman-active vibrational modes (A_g, B_{1g}, B_{2g}, and B_{3g}). It is notable that the Raman spectrum of the synthesized crystals exhibits broad vibrational modes, indicating short-range structural disorder. This characteristic can be related to very rapid kinetics under the synthetic conditions and to intrinsic structural disorder in the lattice, as demonstrated by the Rietveld refinement and first-principles calculations.

Therefore, A_g and B_g are Raman-active modes, and A_u, B_{1u}, B_{2u} and B_{3u} are active vibrational modes in the infrared spectrum. The A and B modes are nondegenerate; subscripts "$_g$" and "$_u$" indicate the parity under inversion in centrosymmetric $Ag_4V_2O_7$ crystals.

Analysis of the micro-Raman spectrum presented in Fig. 3 revealed that the strongest Raman-active modes appear above 770 cm^{-1} with symmetry B_{2g}, dominated by a Raman-active mode at 790 cm^{-1} related to the asymmetric stretching of the distorted trigonal bipyramidal [VO_5] clusters with a B_{1g} or B_{3g} character. Two other B_{2g} Raman-active modes at 810 and 830 cm^{-1} are prominent, derived from the symmetric-stretching vibration of the distorted tetrahedral [VO_4] clusters.

According to group theory, crystals with an orthorhombic structure, a space group (*Pbca*), a point-group symmetry ($D_{(15/2h)}$), and eight molecules per unit cell (Z = 8) exhibit

312 vibrational modes in the center of the Brillouin zone ($\vec{k}=0$), as given by the equation: 55 $\Gamma_{Raman+Infrared(CrystalPrimitive)}$ = {(39 Ag) + (39 B1g) + (39 B2g) + (39 B3g) + [39 Au] + [39 B1u] + [39 B2u] + [39 B3u]}. However, our 3D hexagon-like $Ag_4V_2O_7$ microcrystals have sixteen molecules per unit cell (Z = 16) and display 624 vibrational modes according to the following equation: $\Gamma_{Raman+Infrared(CrystalPrimitive)}$ = {(78 Ag) + (78 B1g) + (78 B2g) + (78 B3g) + [78 Au] + [78 B1u] + [78 B2u] + [78 B3u]}.

The 312 theoretical Raman-active modes are shown in Table S2 (ESI†) and can be organized into two different groups. The first group is composed of modes in the frequency range of 13 to 508 cm^{-1} and is related to lattice phonons and the motion of distorted trigonal bipyramidal [AgO_5] clusters and distorted octahedral/triangular prism [AgO_6] clusters. These modes are basically associated with symmetric and/or asymmetric bending modes of the distorted tetrahedral [VO_4] clusters and distorted trigonal bipyramidal [VO_5] clusters. In the second group, at high frequencies and separated by a phonon gap of nearly 173 cm^{-1}, are the modes corresponding to symmetric and/or asymmetric stretching of the distorted trigonal bipyramidal [VO_5] and distorted tetrahedral [VO_4] clusters.

A comparison of the experimental Raman active modes with the closest theoretically calculated ones is presented in Table S3.† A good agreement between the experimental and calculated Raman-active modes is observed, and these results allow us to confirm the 3D hexagon-like structure of the $Ag_4V_2O_7$ microcrystals obtained in this work. The FE-SEM images of the microcrystals are depicted in Fig. 4(a)–(c). Fig. 4(a) shows a large quantity of small $Ag_4V_2O_7$ microcrystals with a well-defined 3D hexagon-like morphology. Moreover, some of these hexagons have surface defects and are formed by small nanocrystals through a self-assembly process due to the environment during the synthetic process. The microcrystals have an average size of approximately 2.7 μm width with a thickness of about 1 μm, and are formed through the aggregation of several nanocrystals and plates with an average size of approximately 375 nm, as can be seen in Fig. S2(a)–(d) (ESI†). These microcrystals have only 8 faces in the first few minutes of the reaction; however, after 10 min of the reaction at 30 °C, fast growth occurs to afford 3D hexagon-like $Ag_4V_2O_7$ microcrystals with 14 faces, as shown in Fig. S2(e) (ESI†). In Fig. 4(b), a series of $Ag_4V_2O_7$ microcrystals with a more defined shape can be observed due to thermodynamic processes and the chemical synthesis method employed. We also note that these crystals display a regular shape and size, as is evident from Fig. 4(c) and the computationally simulated crystal shape shown in the inset.

Using a specific methodology, which has been applied to study the morphologies of various metal oxides such as SnO_2,[56] $PbMoO_4$,[57] and CaWO4,[58] we developed a combination of experimental studies and first-principles calculations to more deeply investigate the electronic, structural, and energetic properties controlling the morphology and related transformation mechanisms of various metals and metal oxides such as Ag, anatase TiO_2, $BaZrO_3$, and α-Ag_2WO_4 [59] as well as Co_3O_4, Fe_2O_3, and In_2O_3.[60] These cited papers contain a description of the method for the calculation of the surface energies, which were used to characterize the corresponding surface morphologies using Wulff constructions.

The (100), (010), (001), (110), (101), (011), and (111) surfaces of the orthorhombic $Ag_4V_2O_7$ system were modeled by means of unreconstructed (truncated bulk) slab models using the calculated equilibrium geometry (a = 18.752 Å, b = 11.090 Å, c = 13.504 Å) and introducing a vacuum spacing of 15 Å in the z-direction so that the surfaces do not interact with each other. After the corresponding convergence test on the system, slab models containing 8 molecular units were selected, with areas of 149.8 $Å^2$, 153.2 $Å^2$, 208.0 $Å^2$, 294.2 $Å^2$, 256.4 $Å^2$, 327.7 $Å^2$,and 360.3 $Å^2$, for the (100), (010), (001), (110), (101), (011), and (111) surfaces, respectively. Analysis of the theoretical results indicates that the most stable surfaces are the (110), (111), and (101) facets, which can form an ideal morphology (shown in Fig. 4(d)).

When the relative stability of the facets changes (increases or decreases), more than one facet type appears in the resulting morphology, causing morphology variations. A 3D hexagon-like $Ag_4V_2O_7$ morphology with 14 faces is obtained if the surface energies of (110) and (010) increase to 0.60 and 0.68 J m^{-2}, respectively, and the surface energy of (100) decreases to 0.30 J m^{-2} (see Fig. 4(e)). However, a morphology having only 8 faces is produced when the surface energy of (100) decreases to 0.05 J m^{-2} and those of (011) and (001) equal 0.5 J m^{-2}. Thus, variations in the ratios of the values of

the surface energy affect the related morphologies, which can be used to obtain correlations with the experimental results.

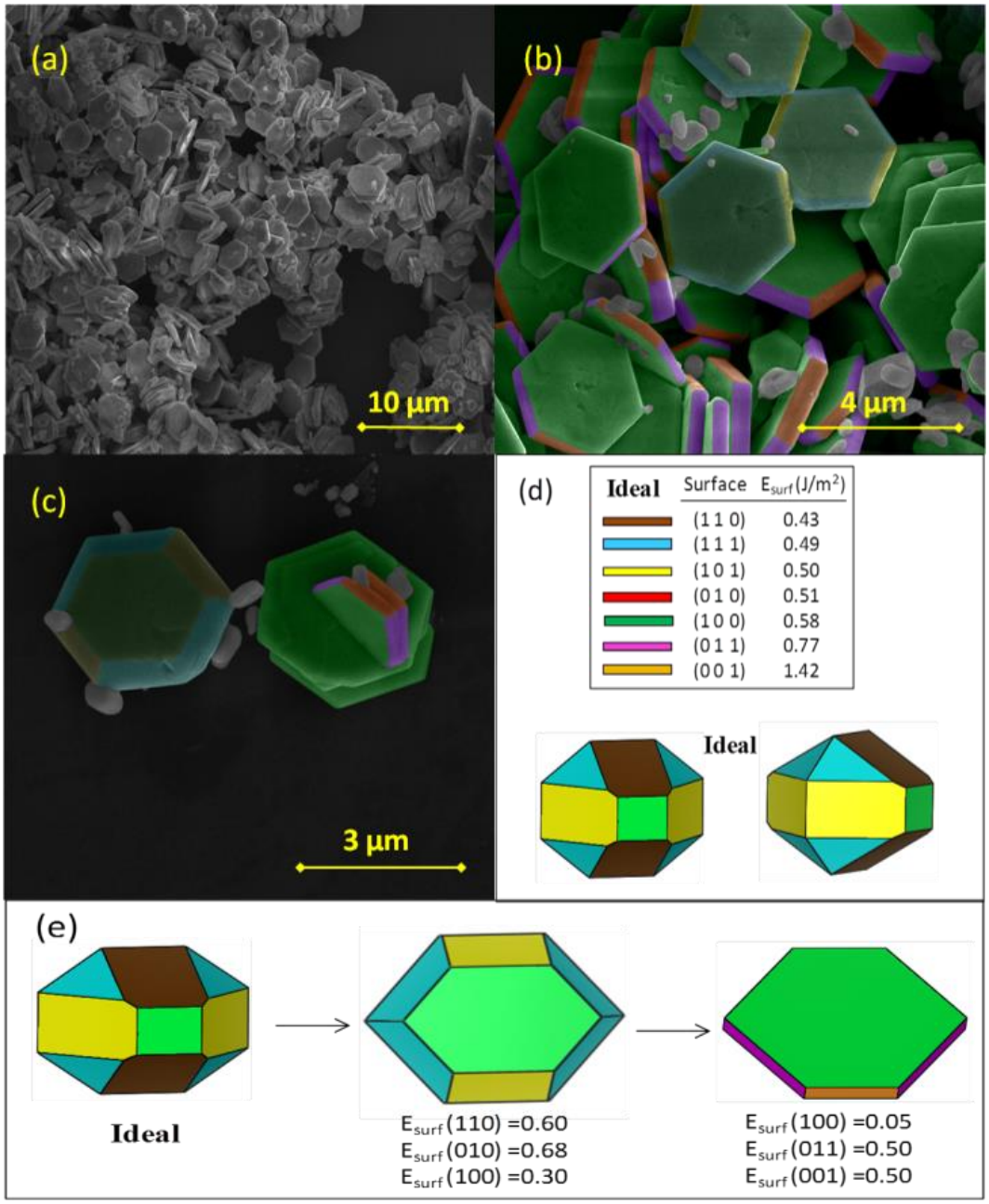

Fig. 4 FE-SEM images of 3D hexagon-like $Ag_4V_2O_7$ microcrystals: (a) low magnification, (b) intermediate magnification and (c) high magnification; (d) computationally simulated crystal shape and the optimized surface energies (J m^{-2}); and (e) theoretical crystal shape for $Ag_4V_2O_7$ microcrystals using the BPE level, respectively.

Fig. 5(a) and (b) show the UV-vis diffuse reflectance spectrum and calculated electronic band structure/density of states (DOS) of 3D hexagon-like $Ag_4V_2O_7$ crystals,

respectively. As seen in Fig. 5(a), an E_{gap} value of 2.45 eV was obtained for our 3D hexagon-like $Ag_4V_2O_7$ microcrystals, as calculated by extrapolating the linear portion of the UV-vis curve. In principle, we believe that this behavior is related to the presence of intermediary energy levels between the valence band (VB) and the conduction band (CB), since the exponential optical absorption edge and E_{gap} are controlled by the degree of structural order–disorder in the lattice. Calculations yield a direct band gap value of 2.86 eV, as is revealed in Fig. 5(b); the band structures of the 3D hexagon-like $Ag_4V_2O_7$ micro-crystals are characterized by well-defined direct electronic transitions, which is a typical nature of crystalline semiconductor materials. Fundamentally, the top of the valence band (VB) as well as the bottom of the conduction band (CB) are in the same Γ points in the Brillouin zone and, for a simplified description, this difference can be mainly attributed to the distortions of both tetrahedral/trigonal bipyramidal [VO_z] (z =4 and 5) clusters and trigonal bipyramidal/octahedral [AgO_y] (y = 6 and 5) clusters at short- and medium-range, and is presented in Fig. 5(b).

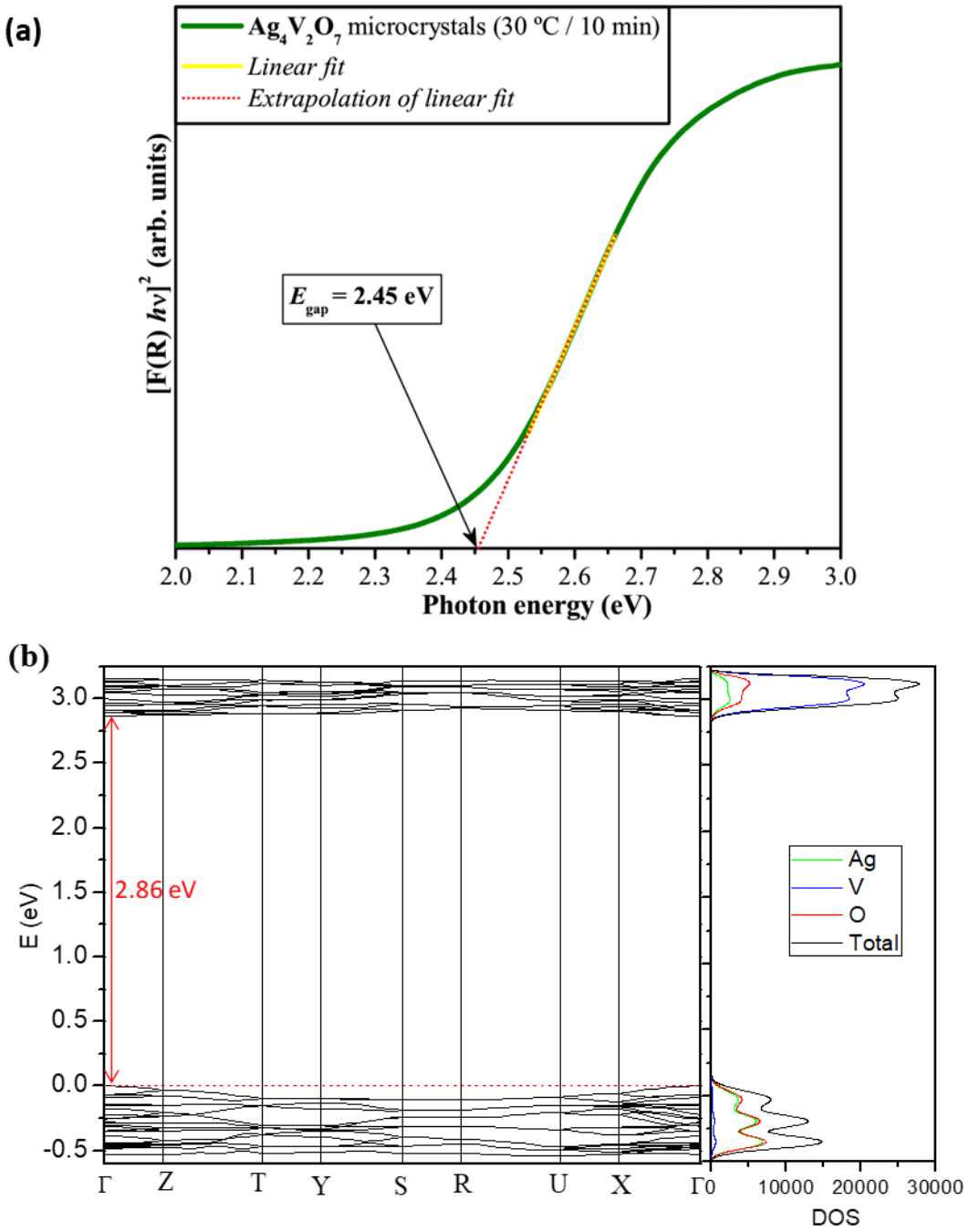

Fig. 5 (a) UV-vis spectrum and (b) band structure/DOS of 3D hexagon-like $Ag_4V_2O_7$ microcrystals, respectively.

At this point, it is important to note that determination of the structural order–disorder in a crystalline solid plays a crucial role in the understanding of the relation between its physical properties and its electronic structure, and advanced methodologies allow nowadays for the precise control of the composition and properties of nanomaterials.[61,62] For a given material, structural disorder can present useful properties, such as ferroelectricity, piezoelectricity, and nonlinear optical behavior.[63–66] Therefore, it is important to create disorder in order to obtain new materials with unique physical

properties that would be otherwise inaccessible in well-ordered crystal structures.[67] In this context, PL properties are environment-sensitive and significantly affected by the degree of structural order–disorder that accompanies the changes in crystal size and morphology during the synthetic process.

The PL spectrum at room temperature of $Ag_4V_2O_7$ micro-crystals is shown in Fig. 6. The PL spectrum exhibits a typical broad band profile, which can be associated with multiphonon or multilevel processes, i.e., a solid system where relaxation occurs by several pathways that involve the participation of numerous energy states within the band gap. The PL spectrum covers a broad range of wavelengths, from 350 to 600 nm, centered at 450 nm in the blue region of the visible spectra for the 3D hexagon-like $Ag_4V_2O_7$ microcrystals (see Fig. 6).

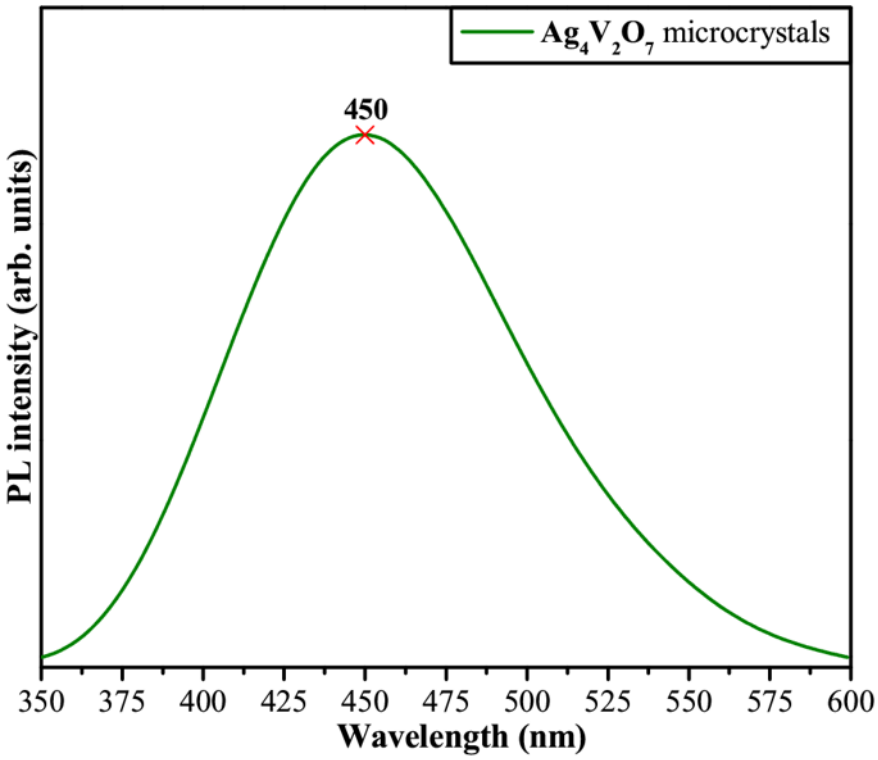

Fig. 6 PL emission spectrum of 3D hexagon-like $Ag_4V_2O_7$ microcrystals.

The photoluminescence emission of vanadate-based compounds has been associated with charge transfer transitions from the oxygen ligands O^{2-} to the central vanadium ions V^{5+} in $[VO_4]$ tetrahedra, as well as complex cluster vacancies and/or modified lattices.[68,69] However, all these explanations are directly associated with VO^{3-} ions (while, Ag V O is a crystalline solid composed of a structural framework formed by interconnected ($[VO_4]$–$[AgO_5]$–$[VO_4]$–$[AgO_6]$⋯) clusters (see Fig. 2(b)). Therefore, we can assume that the distorted tetrahedral $[VO_4]$ clusters and distorted trigonal

bipyramidal [VO_5] clusters are mainly responsible through electronic transitions between the VB and CB.

As there is an interconnection between the distorted trigonal bipyramidal [AgO_5] clusters and the distorted octahedral [AgO_6] clusters in the orthorhombic lattice, it is possible to conclude that any distortion caused on the [VO_4] and [VO_5] clusters also promotes a slight deformation of the O–Ag–O bonds that form part of the chain. The association of different vanadium and silver clusters yields a wide range of polarization charges with the formation of electron–hole pairs between clusters. In instances involving electronic conduction properties, these clusters are able to present cluster-to-cluster charge transfer (CCCT) from vanadium to silver (or vice-versa) by means of excitations involving electronic transitions. This CCCT mechanism induces the formation of different energy levels within the forbidden band gap (structural order–disorder effect). Particularly, this phenomenon has its origin during the crystal formation and organization stages, which are directly dependent on interactions between tetrahedral/trigonal bipyramidal [VO_z] (z = 4 and 5) clusters and trigonal bipyramidal/octahedral [AgO_y] (y = 5 and 6) clusters. Therefore, these structural defects promote a symmetry break, causing polarization of the structure by electronic charge transfer from ordered (o) to disordered (d) clusters (formation of electron–hole pairs). The corresponding equations are presented in the ESI,† S4.

The PL bands arise from photogenerated electron–hole pair processes and the electronic transition between the VB (2p levels of O atoms and 4d levels of Ag atoms) and the CB (3d levels of V atoms). Breaking symmetry processes in these clusters with distortions and tilts create a huge number of different structures and subsequently different material properties related to local (short), intermediate, and long-range structural order–disorder. Finally, our data indicated that the 3D hexagon-like $Ag_4V_2O_7$ microcrystals have a very short luminescence lifetime in the order of hundreds of nanoseconds (Fig. S3†).

4. Conclusions

In summary, new research studies on the synthesis of $Ag_4V_2O_7$ crystals with novel properties have attracted great attention because of the variety of their potential applications. This study not only provides new information on the geometry, cluster coordination, and electronic structure of $Ag_4V_2O_7$ microcrystals, but also illustrates the potential of combining experimental techniques and first-principles DFT calculations. This

combination led us to develop a systematic procedure to study the structure and electronic DOS of $Ag_4V_2O_7$. We found that it exhibits an orthorhombic structure, formed by two types of clusters of V atoms, [VO_4] and [VO_5], and two types of clusters of Ag atoms, [AgO_5] and [AgO_6]. These clusters act as building blocks for the $Ag_4V_2O_7$ structure. Features in the Raman spectra were identified through comparison with calculated vibrational frequencies, and this confirmed the predicted structure of this material. The UV-vis spectrum indicated that $Ag_4V_2O_7$ microcrystals have a direct band gap with a value of E_{gap} = 2.45 eV. The luminescence lifetime is very short in the order of hundreds of nanoseconds. The present work provides a new direction toward the design of this crystalline material and the search for practical applications in, for example, biology, catalysis, and photoluminescent materials. This knowledge may help in developing effective processing routines to enhance the performance of bulk heterojunction solar cells. With the combined insight provided by multiscale simulations and experiments, it may be possible to develop effective tempering routes to fine-tune the electronic structure of organic semiconductor materials. This would allow the development of nanostructure arrays with great potential in technological applications such as optical sensors and photoelectronic materials.

Acknowledgements

The authors acknowledge the financial support of the following agencies: CAPES (PNPD-1268069), FAPESP (2013/07296-2;2013/26671-9), CNPq (304531/2013-8), Generalitat Valenciana for PrometeoII/2014/022 and ACOMP/2014/270, Ministerio de Economia y Competitividad, project CTQ2012-36253-C03-02, and the Spanish Brazilian program (PHBP14-00020). We also acknowledge the Servei Informática, Universitat Jaume I for the generous allotment of computer time. J. A. acknowledges the Ministerio de Economia y Competitividad, “Salvador Madariaga” program, PRX15/00261. L. G. acknowledges Banco Santander (Becas Iberoamérica: Jóvenes profesores e investigadores)

References

1 K. J. Takeuchi, A. C. Marschilok, S. M. Davis, R. A. Leising and E. S. Takeuchi, Coord. Chem. Rev., 2001, 219, 283.

2 R. Konta, H. Kato, H. Kobayashi and A. Kudo, Phys. Chem. Chem. Phys., 2003, 5, 3061.

3 J. Ren, W. Wang, M. Shang, S. Sun, L. Zhang and J. Chang, J. Hazard. Mater., 2010, 183, 950.

4 X. Hu, C. Hu and J. Qu, Mater. Res. Bull., 2008, 43, 2986.

5 C. M. Huang, G. T. Pan, Y. C. M. Li, M. H. Li and T. C. K.
Yang, Appl. Catal., A, 2009, 358, 164.

6 C. M. Huang, K. W. Cheng, G. T. Pan, W. S. Chang and T. C. K. Yang, Chem. Eng. Sci., 2010, 65, 148–152.

7 L. C. Chen, G. T. Pan, T. C. K. Yang, T. W. Chung and C. M. Huang, J. Hazard. Mater., 2010, 178, 644.

8 Z. Chen, S. Gao, R. Li, M. Wei, K. Wei and H. Zhou, Electrochim. Acta, 2008, 53, 8134.

9 J. Wang, X. Yang, J. Chen, J. Xian, S. Meng, Y. Zheng, Y. Shao and D. Li, J. Am. Ceram. Soc., 2014, 97, 267.

10 J. Wang, J. Chen, Y. Yu, W. Yu, X. Meng, J. Chen and D. Li, CrystEngComm, 2015, 17, 6661.

11 L. Mai, L. Xu, Q. Gao, C. Han, B. Hu and Y. Pi, Nano Lett., 2010, 10, 2604.

12 W. D. Chemelewski, O. Mabayoje and C. B. Mullins, J. Phys. Chem. C, 2015, 119, 26803.

13 L. Liang, Y. Xu, Y. Lei and H. Liu, Nanoscale, 2014, 6, 3536.

14 S. Liang, J. Zhou, X. Zhang, Y. Tang, G. Fang, T. Chen and X. Tan, CrystEngComm, 2013, 15, 9869.

15 L. Liang, H. Liu and W. Yang, Nanoscale, 2013, 5, 1026.

16 Y. Sang, L. Kuai, C. Chen, Z. Fang and B. Geng, ACS Appl. Mater. Interfaces, 2014, 6, 5061.

17 Q. Zhu, W. S. Wang, L. Lin, G. Q. Gao, H. L. Guo, H. Du and A.-W. Xu, J. Phys. Chem. C, 2013, 117, 5894.

18 M. R. Parida, C. Vijayan, C. S. Rout, C. S. S. Sandeep and R. Philip, Appl. Phys. Lett., 2012, 100, 1211191.

19 P. Ju, H. Fan, B. Zhang, K. Shang, T. Liu, S. Ai and D. Zhang, Sep. Purif. Technol., 2013, 109, 107.

20 H. Xu, H. Li, L. Xu, C. Wu, G. Sun, Y. Xu and J. Chu, Ind. Eng. Chem. Res., 2009, 48, 10771.

21 H. Shi, Z. Li, J. Kou, J. Ye and Z. Zou, J. Phys. Chem. C, 2011, 115, 145.

22 S. Kittaka, S. Nishida and T. Ohtani, J. Solid State Chem., 2002, 169, 139.

23 R. Masse, M. T. Averbuchpouchot, A. Durif and J. C. Guitel, Acta Crystallogr., Sect. C: Cryst. Struct. Commun., 1983, 39, 1608.
24 T. A. Albrecht, C. L. Stern and K. R. Poeppelmeier, Inorg. Chem., 2007, 46, 1704.
25 R. Ran, J. G. McEvoy and Z. Zhang, Mater. Res. Bull., 2016, 74, 140.
26 C. Belver, C. Adan, S. Garcia-Rodriguez and M. Fernandez- Garcia, Chem. Eng. J., 2013, 224, 24.
27 V. M. Longo, C. C. De Foggi, M. M. Ferrer, A. F. Gouveia, R. S. Andre, W. Avansi, C. E. Vergani, A. L. Machado, J. Andres, L. S. Cavalcante, A. C. Hernandes and E. Longo, J. Phys. Chem. A, 2014, 118, 5769.
28 P. S. Lemos, A. Altomare, A. F. Gouveia, I. C. Nogueira, L. Gracia, R. Llusar, J. Andres, E. Longo and L. S. Cavalcante, Dalton Trans., 2016, 45, 1185.
29 Y. V. B. De Santana, L. Matos, G. Henrique, A. P. Cruvinel, C. Perrin, J. Andrés, J. A. Varela and E. Longo, Nanomater. Nanotechnol., 2014, 4, 22–31.
30 E. Longo, D. P. Volanti, V. M. Longo, L. Gracia, I. C.Nogueira, M. A. P. Almeida, A. N. Pinheiro, M. M. Ferrer, L. S. Cavalcante and J. Andres, J. Phys. Chem. C, 2014, 118,1229.
31 L. F. da Silva, A. C. Catto, W. Avansi Jr., L. S. Cavalcante, J. Andres, K. Aguir, V. R. Mastelaro and E. Longo, Nanoscale, 2014, 6, 4058.
32 R. A. Roca, J. C. Sczancoski, I. C. Nogueira, M. T. Fabbro, H. C. Alves, L. Gracia, L. P. S. Santos, C. P. De Sousa, J. Andrés, G. E. Luz, E. Longo and L. S. Cavalcante, Catal. Sci.Technol., 2015, 5, 4091.
33 M. T. Fabbro, C. Saliby, L. R. Rios, F. A. La Porta, L. Gracia, M. S. Li, J. Andres, L. P. S. Santos and E. Longo, Sci. Technol. Adv. Mater., 2015, 16, 65002.
34 G. Botelho, J. C. Sczancoski, J. Andres, L. Gracia and E. Longo, J. Phys. Chem. C, 2015, 119, 6293.
35 G. Botelho, J. Andres, L. Gracia, L. S. Matos and E. Longo, ChemPhysChem, 2015, 81, 202.
36 R. Dovesi, V. R. Saunders, C. Roetti, R. Orlando, C. M. Zicovich-Wilson, F. Pascale, B. Civalleri, K. Doll, N. M.Harrison, I. J. Bush, P. D'Arco, M. Llunell, M. Causà and Y. Noël, Crystal14 User's Manual, University of Torino, Torino, 2014.
37 F. Cora, A. Patel, N. M. Harrison, R. Dovesi and C. R. A. Catlow, J. Am. Chem. Soc., 1996, 118, 12174.
38 CRYSTAL - Basis Sets Library, http://www.crystal.unito.it/basis-sets.php, (accessed March, 2016).

39 S. Grimme, J. Comput. Chem., 2006, 27, 1787.

40 T. Bucko, J. Hafner, S. Lebegue and J. G. Angyan, J. Phys.Chem. A, 2010, 114, 11814.

41 G. Kresse and J. Hafner, Phys. Rev. B: Condens. Matter Mater. Phys., 1994, 49, 14251.

42 J. Heyd, G. E. Scuseria and M. Ernzerhof, J. Chem. Phys., 2003, 118, 8207.

43 A. H. Reshak, O. V. Parasyuk, A. O. Fedorchuk, H. Kamarudin, S. Auluck and J. Chyský, J. Phys. Chem. B, 2013, 117, 15220.

44 A. H. Reshak, X. Chen, S. Auluck, H. Kamarudin, J. Chyský, A. Wojciechowski and I. V. Kityk, J. Phys. Chem. B, 2013, 117, 14141.

45 A. H. Reshak, H. Kamarudin, I. V. Kityk and S. Auluck, J. Phys. Chem. B, 2012, 116, 13338.

46 A. H. Reshak, H. Kamarudin and S. Auluck, J. Phys. Chem. B, 2012, 116, 4677.

47 G. E. Davydyuk, O. Y. Khyzhun, A. H. Reshak, H. Kamarudin, G. L. Myronchuk, S. P. Danylchuk, A. O. Fedorchuk, L. V. Piskach, M. Yu. Mozolyukf and O. V. Parasyukf, Phys. Chem. Chem. Phys., 2013, 15, 6965.

48 A. H. Reshak, D. Stys, S. Auluck and I. V. Kityk, Phys. Chem.Chem. Phys., 2011, 13, 2945.

49 H. M. Rietveld, J. Appl. Crystallogr., 1969, 2, 65.

50 H. M. Rietveld, Acta Crystallogr., 1967, 22, 151.

51 A. C. Larson and R. B. Von Dreele, General structure analysis system (GSAS), Los Alamos National Laboratory, 2001, pp. 124–213.

52 K. Momma and F. Izumi, J. Appl. Crystallogr., 2011, 44, 1272.

53 K. Momma and F. Izumi, J. Appl. Crystallogr., 2008, 41, 653.

54 L. S. Cavalcante, M. A. P. Almeida, W. Avansi Jr., R. L. Tranquilin, E. Longo, N. C. Batista, V. R. Mastelaro and M. Siu Li, Inorg. Chem., 2012, 51, 10675.

55 D. L. Rousseau, R. P. Bauman and S. P. S. Porto, J. Raman Spectrosc., 1981, 10, 253.

56 D. G. Stroppa, L. A. Montoro, A. Campello, L. Gracia, A. Beltran, J. Andres, E. R. Leite and A. J. Ramirez, Phys. Chem. Chem. Phys., 2014, 16, 1089.

57 M. R. D. Bomio, R. L. Tranquilin, F. V. Motta, C. A. Paskocimas, R. M. Nascimento, L. Gracia, J. Andres and E. Longo, J. Phys. Chem. C, 2013, 117, 21382.

58 V. M. Longo, L. Gracia, D. G. Stroppa, L. S. Cavalcante, M. Orlandi, A. J. Ramirez, E. R. Leite, J. Andres, A. Beltran, J. A.Varela and E. Longo, J. Phys. Chem. C, 2011, 115, 20113.
59 J. Andres, L. Gracia, A. F. Gouveia, M. M. Ferrer and E. Longo, Nanotechnology, 2015, 26, 405703.
60 M. Ferrer, A. Gouveia, L. Gracia, E. Longo and J. Andrés, Modell. Simul. Mater. Sci. Eng., 2016, 24, 25007.
61 D. Koziej, A. Lauria and M. Niederberger, Adv. Mater., 2014, 26, 235.
62 M. V. Kovalenko, L. Manna, A. Cabot, Z. Hens, D. V. Talapin, C. R. Kagan, V. I. Klimov, A. L. Rogach, P. Reiss, D. J. Milliron, P. Guyot-Sionnnest, G. Konstantatos, W. J. Parak, T. Hyeon, B. A. Korgel, C. B. Murray and W. Heiss, ACS Nano, 2015, 9, 1012.
63 J. F. Nye, Physical Properties of Crystals: Their Representation by Tensors and Matrices, Oxford University Press, Oxford, 1985.
64 T. Vehoff, B. Baumeier, A. Troisi and D. Andrienko, J. Am. Chem. Soc., 2010, 132, 11702.
65 T. Vehoff, Y. S. Chung, K. Johnston, A. Troisi, D. Y. Yoon and D. Andrienko, J. Phys. Chem. C, 2010, 114, 10592.
66 M. Mas-Torrent, P. Hadley, S. T. Bromley, X. Ribas, J. Tarres, M. Mas, E. Molins, J. Veciana and C. Rovira, J. Am. Chem. Soc., 2004, 126, 8546.
67 A. B. Cairns and A. L. Goodwin, Chem. Soc. Rev., 2013, 42, 4881.
68 Y. Pu, Y. Huang, T. Tsuboi, H. Cheng and H. J. Seo, RSC Adv., 2015, 5, 73467.
69 A. D. J. David, G. S. Muhammad and V. Sivakumar, Chin. J. Struct. Chem., 2015, 5, 393.

Supplementary Information

Disclosing the Electronic Structure and Optical Properties of $Ag_4V_2O_7$ crystals: Experimental and Theoretical Insights

R.C. de Oliveira[a], L. Gracia[b], M. Assis[a], M. Siu Li[c], J. Andres[b], E. Longo[d], L.S. Cavalcante[e]*

[a]*INCTMN-UFSCar, Universidade Federal de São Carlos, P.O. Box 676, 13565–905, São Carlos, SP, Brazil.*

[b]*Departament de Química Física i Analítica, Universitat Jaume I, 12071, Castelló de la Plana, Spain.*

[c]*IFSC-Universidade de São Paulo, P.O. Box 369, 13560-970 São Carlos, São Paulo, Brazil*

[d]*INCTMN-UNESP, Universidade Estadual Paulista, P.O. Box 355, 14801–907 Araraquara, SP, Brazil*

[e]*PPGQ-Universidade Estadual do Piauí, Rua João Cabral, 2231, P.O. Box 381, 64002–150, Teresina, PI, Brazil.*

**laeciosc@gmail.com;*

Experimental details

The precursors utilized in this synthesis were silver nitrate, $AgNO_3$ (99,0% purity, Synth) and ammonium monovanadate, NH_4VO_3 (99% purity, Aldrich). Initially, 1×10^{-3} mol de NH_4VO_3 were dissolved in 60 mL distilled water at 30°C, under magnetic stirring for 15 minutes. Then, 1×10^{-3} mol of $AgNO_3$ were dissolved in 15 mL distilled water, under magnetic stirring for 15 minutes, to this solution was added a few drops of ammonium hydroxide (NH_4OH) (30% in NH_3, Synth) until the solution becomes clear. Both solutions were quickly mixed, promoting the instantaneous formation of solid $Ag_4V_2O_7$ precipitates (orange coloration). To accompany the change of morphologies, the PM was performed at 30 ºC for 10 min. The precipitate was centrifuged, washed with distilled water several times, and dried in a conventional furnace at 60 ºC for some hours.

Characterization

X-ray diffraction using a Rigaku-DMax/2500PC (Japan) with Cu Kα radiation (λ = 1.5406 Å) in the 2θ range from 10° to 80° with a scanning rate of 0.02°/min. Micro-Raman spectroscopy was carried out using an T64000 spectrometer (Horiba obin-Yvon, Japan) coupled to a CCD Synapse detector and an argon-ion laser, operating at 514 nm with maximum power of 7 mW. The spectra were measured in the range from 100 cm^{-1} to 1100 cm^{-1}. UV-vis spectra were obtained in a Varian spectrophotometer model Cary 5G (USA) in diffuse reflection mode. The morphologies were investigated with a field emission scanning electron microscopy (FE-SEM) Supra 35-VP Carl Zeiss (Germany) operated in 15 KV. The PL measurements were performed with a Monospec 27 monochromator Thermal Jarrel Ash (USA) coupled to a R446 photomultiplier Hamamatsu Photonics (Japan). A krypton ion laser Coherent Innova 90 K (USA) (λ = 350 nm) was used as excitation source, keeping its maximum output power at 500 mW. All experiments measurements were performed at room temperature.

Theoretical Calculations

Calculations on the periodic $Ag_4V_2O_7$ structure were performed with the CRYSTAL14 sofware package /Dovesi R.; Saunders, V. R.; Roetti, C.; Orlando, R.; Zicovich-Wilson, C. M.; Pascale, F.; Civalleri, B.; Doll, K.; Harrison, N. M.; Bush, I. J.; D'Arco, P.; Llunell, M.; Causà M.; Noël Y., *Crystal14 User's Manual*. University of Torino: Torino, 2014./ Tungsten was described by a large-core ECP, derived by Hay and Wadt, and modified by Cora *et al*. /Cora, F.; Patel, A.; Harrison, N. M.; Dovesi, R.; Catlow, C. R. A. An Ab Initio Hartree-Fock Study of the Cubic and Tetragonal Phases of Bulk Tungsten Trioxide. *J. Am. Chem. Soc.* **1996**, *118*, 12174-12182./ Silver and oxygen centers were described using HAYWSC-311d31G and O (6-31d1G) basis sets, respectively, which were taken from the Crystal web site./ http://www.crystal.unito.it/Basis_Sets/Ptable.html/ A Range-separated hybrid functional, the screened-Coulomb HSE06 was used in order to give the accurate band gaps for the computed structures. The diagonalization of the Fock matrix was performed at adequate *k*-points grids in the reciprocal space. The thresholds controlling the accuracy of the calculation of the Coulomb and exchange integrals were set to10^{-8} and 10^{-14}, and the percent of Fock/Kohn-Sham matrices mixing was set to 40 (IPMIX keyword)./Dovesi R.; Saunders, V. R.; Roetti, C.; Orlando, R.; Zicovich-Wilson, C. M.; Pascale, F.; Civalleri, B.; Doll, K.; Harrison, N. M.; Bush, I. J.; D'Arco, P.; Llunell, M.; Causà M.; Noël Y., *Crystal14 User's Manual*. University of Torino: Torino, 2014./ The empirical correction scheme to energy that considers the long-range dispersion contributions proposed by Grimme/ S. Grimme, *Journal of Computational Chemistry* 2006, *27*, 1787-1799/ and implemented by Bucko et al./ T. Bucko, J. Hafner, S. Lebegue, J. G. Angyan, *Journal of Physical Chemistry A* 2010, *114*, 11814-11824/ for periodic systems was used. In the relaxed configuration, the forces on the atoms are less than 0.0001 hartree/bohr = 0.005 eV/Å, and deviations of the stress tensor from a diagonal hydrostatic form are less than 0.1 GPa. The band structure and the density of states (DOS) projected on atoms and orbitals of bulk $Ag_4V_2O_7$ was constructed along the appropriate high-symmetry directions of the corresponding irreducible Brillouin zone. The vibrational-frequencies calculation in CRYSTAL is performed at the Γ-point within the harmonic approximation, and the dynamic matrix is computed by the numerical evaluation of the first derivative of analytical atomic gradients.

a)

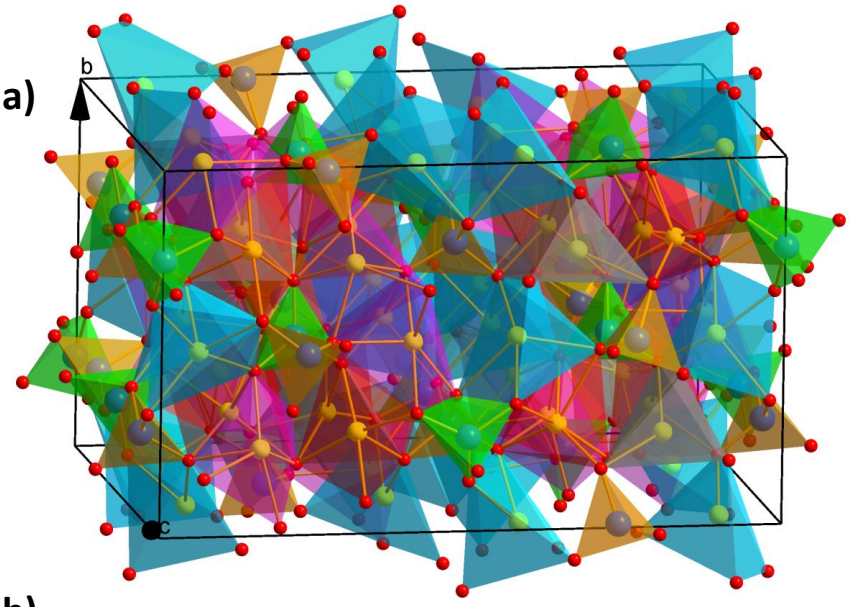

Atom	Lig	Dmin	Dmax
Ag1	5	2.271	2.636
Ag2	6	2.31	2.906
Ag3	6	2.317	2.657
Ag4	6	2.366	2.96
Ag5	6	2.438	2.982
Ag6	6	2.332	2.811
Ag7	5	2.255	2.672
Ag8	5	2.336	2.494
V1	5	1.708	2.158
V2	4	1.708	1.769
V3	4	1.707	1.788
V4	5	1.698	2.258

b)

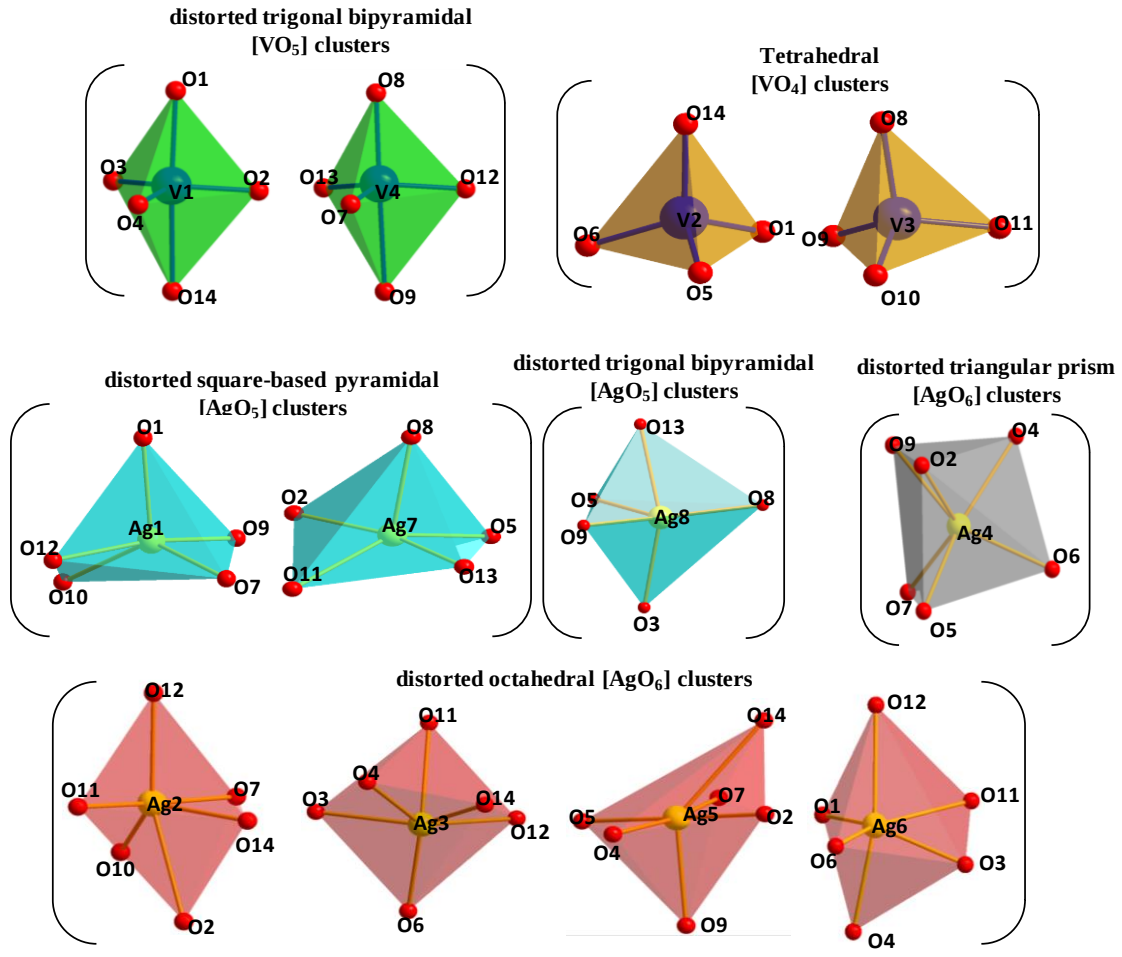

Fig. S1: (a) show a schematic representation of orthorhombic $Ag_4V_2O_7$ unit cell in which the different clusters, i.e. the local coordination of V and Ag atoms are depicted. (b) molecular geometry, and coordination of each cluster in $Ag_4V_2O_7$ crystals.

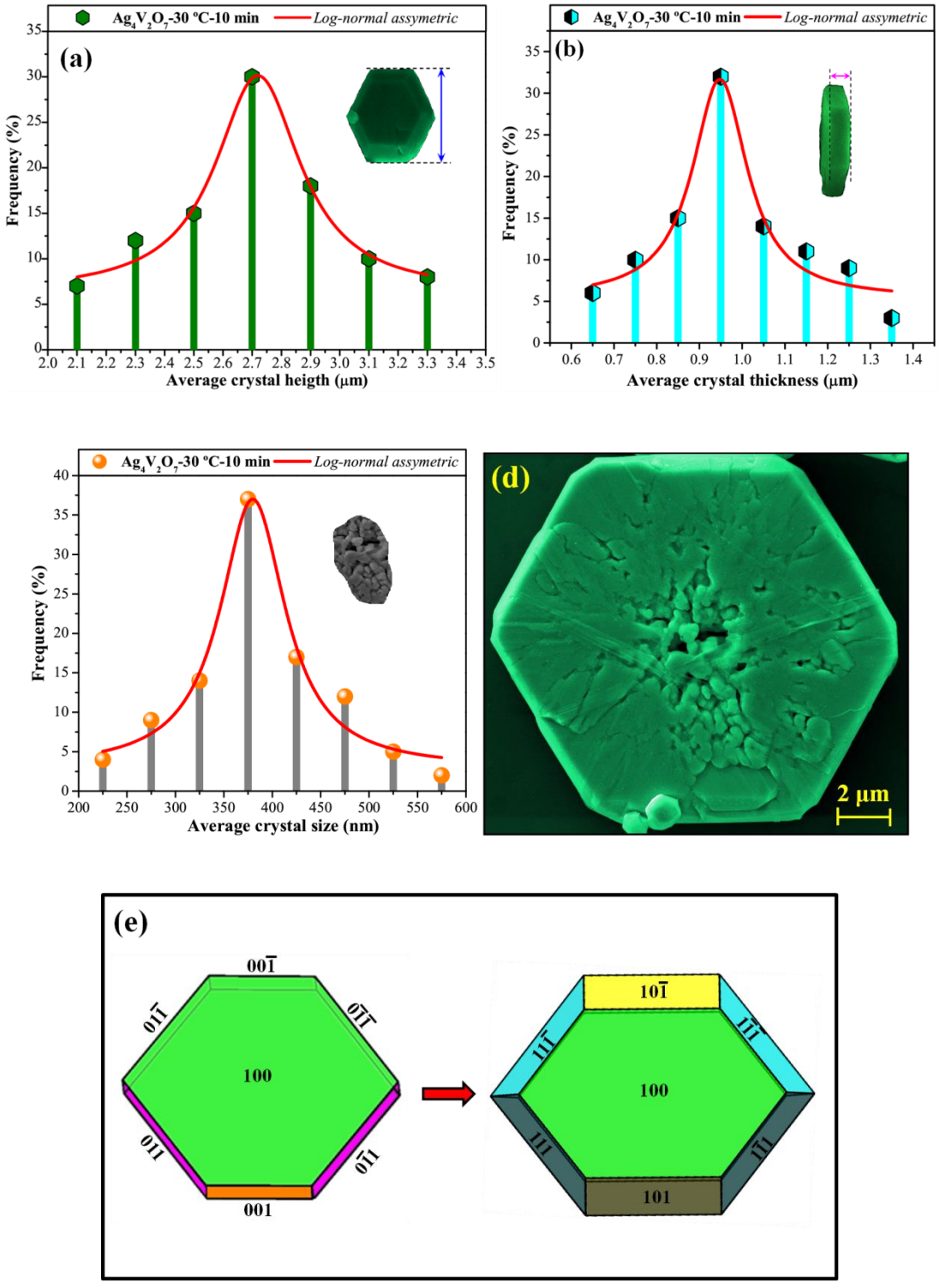

Figs. S2: (a) Average crystal height distribution and (b) Average crystal thickness distribution, (c) Average crystal size distribution of small presents into the $Ag_4V_2O_7$ microcrystals (d) FE-SEM images of an individual $Ag_4V_2O_7$ microcrystals and (e) Crystal

shape simulated computationally for 3D hexagons-like $Ag_4V_2O_7$ microcrystals with 8 faces and 14 faces, respectively.

Table 1: (a) Lattice parameters, unit cell volume, atomic coordinates, and site occupation obtained by rietveld refinement data for the 3D hexagons-like $Ag_4V_2O_7$ microcrystals obtained at 30 ºC for 10 min and (b) Data obtained from DFT calculations for $Ag_4V_2O_7$ microcrystals

$Ag_4V_2O_7$ (Rietveld refinement)				
Atoms	Wyckoff	*x*	*y*	*z*
Ag1	8c	0.91648	0.00724	0.88767
Ag2	8c	0.91424	0.00080	0.12302
Ag3	8c	0.17269	0.22475	0.90064
Ag4	8c	0.17000	0.75148	0.12172
Ag5	8c	0.83569	0.24967	0.62928
Ag6	8c	0.33870	0.74855	0.65735
Ag7	8c	0.08971	0.49878	0.14015
Ag8	8c	0.08720	0.50628	0.87029
V1	8c	0.25970	0.98828	0.75072
V2	8c	0.25995	-0.01414	0.01694
V3	8c	-0.00048	0.75612	0.72982
V4	8c	0.49883	0.25563	0.49753
O1	8c	0.21073	0.47325	0.62457
O2	8c	0.32996	0.41715	0.74135
O3	8c	0.17766	0.09133	0.30430
O4	8c	0.25982	0.35742	0.26332

O5	8c	0.16672	0.56642	0.00812
O6	8c	0.29759	0.84466	0.02677
O7	8c	0.43561	0.33066	-0.00217
O8	8c	0.02548	0.18388	0.39472
O9	8c	0.06760	0.81591	0.22975
O10	8c	-0.01673	0.85708	0.81366
O11	8c	0.42149	0.66246	0.76791
O12	8c	0.41501	0.83280	0.51010
O13	8c	0.00632	0.36942	0.08602
O14	8c	0.28365	0.99945	0.41432

a = 18.7993(9) Å, b = 10.85376(3) Å, c = 13.9028(4) Å, α = β = γ = 90°,

V = 2836.77(18) Å^3, R_{Bragg} = 3.56%, R_{wp} = 7.74%, R_p (%) = 5.62%, χ^2 = 1.427 and S = 1.1945

$Ag_4V_2O_7$ (DFT calculations)				
Atoms	Wyckoff	x	y	z
Ag1	8c	-0.0857	-0.0006	-0.1104
Ag2	8c	-0.0787	0.0127	0.1284
Ag3	8c	0.1757	0.2079	-0.1103
Ag4	8c	0.1796	-0.2323	0.1006
Ag5	8c	-0.1634	0.2395	-0.3506
Ag6	8c	0.3427	-0.2514	-0.3499
Ag7	8c	0.0933	-0.4904	0.1186
Ag8	8c	0.0773	0.4713	-0.1333
V1	8c	0.2508	-0.0272	-0.2612

V2	8c	0.2629	-0.0125	-0.0077
V3	8c	0.0007	-0.2719	-0.2651
V4	8c	0.4965	0.2472	0.4873
O1	8c	0.2183	0.4619	-0.4
O2	8c	0.3279	0.392	-0.2813
O3	8c	0.1784	0.1043	0.2871
O4	8c	0.2539	0.3731	0.2397
O5	8c	0.1649	-0.4214	-0.0264
O6	8c	0.2895	-0.1587	0.0126
O7	8c	0.4130	0.321	-0.01
O8	8c	-0.0054	0.1934	0.3806
O9	8c	0.0716	-0.1316	0.2374
O10	8c	0.0025	-0.1718	-0.168
O11	8c	0.4218	-0.3497	-0.2349
O12	8c	0.4293	-0.157	0.499
O13	8c	0.0063	0.3818	0.071
O14	8c	0.2897	0.0075	0.3875

a = 18.752 Å, b = 11.090 Å, c = 13.504 Å, α = β = γ = 90°, V = 2808.29 Å^3

Table S2: Calculated Raman-active modes from optimized orthorhombic structure of $Ag_4V_2O_7$ crystals.

mode	ω (cm^{-1})	mode	ω (cm^{-1})	mode	ω (cm^{-1})	mode	ω (cm^{-1})	mode	ω (cm^{-1})	mode	ω (cm^{-1})	mode	ω (cm^{-1})	mode	ω (cm^{-1})
Ag	13.91	Ag	65.13	B1g	93.51	B3g	162.30	B1g	243.09	B2g	351.35	Ag	440.05	B3g	800.86
B1g	27.48	B3g	66.58	Ag	94.33	B2g	163.15	Ag	244.58	Ag	351.85	B3g	444.25	B1g	803.52
B2g	31.25	B2g	67.04	B3g	94.36	B2g	165.83	B2g	245.56	B1g	357.74	B2g	448.70	Ag	807.52
B1g	35.55	Ag	67.30	Ag	96.19	Ag	165.99	B1g	251.69	Ag	358.96	B3g	449.04	B2g	809.54
B2g	36.73	B1g	67.50	B2g	97.44	B1g	168.27	B2g	261.91	B1g	360.05	B1g	452.14	B2g	810.08
Ag	37.75	B2g	67.74	B3g	98.73	B2g	172.09	B3g	263.12	B3g	361.69	Ag	454.01	B3g	819.43
B3g	38.46	B2g	69.31	B2g	100.03	B1g	173.29	Ag	263.35	B2g	365.35	B2g	455.92	B1g	819.78
Ag	39.25	B1g	69.40	B1g	100.59	Ag	174.56	B3g	272.86	B1g	367.51	B3g	459.63	Ag	819.90
B1g	40.92	B3g	69.68	B3g	104.06	B3g	175.17	B1g	274.15	Ag	368.16	B3g	468.11	B1g	827.30
B3g	42.43	B1g	70.81	B1g	106.94	B3g	175.64	B2g	274.22	B3g	368.43	B1g	471.55	B2g	827.99
Ag	42.78	Ag	72.34	Ag	107.86	B1g	176.92	Ag	275.88	B2g	370.82	B2g	473.45	Ag	829.05
B3g	44.09	B2g	72.45	B2g	107.88	B1g	181.91	B3g	279.99	B3g	372.51	Ag	473.56	B3g	833.82
Ag	44.80	B3g	72.50	B3g	107.90	B2g	184.57	B1g	282.51	Ag	377.91	B2g	490.26	Ag	838.04
B3g	46.44	B1g	73.38	B3g	110.86	B3g	188.11	B2g	284.62	B1g	380.49	B1g	490.44	B2g	839.60
Ag	47.03	Ag	74.16	Ag	111.41	B1g	188.19	B1g	290.14	B3g	381.60	B3g	505.31	B3g	840.88
B2g	47.39	Ag	74.54	Ag	115.31	B2g	189.27	B2g	291.91	B2g	382.61	Ag	508.40	B1g	840.99
B2g	48.20	B2g	74.55	B2g	117.54	Ag	192.36	Ag	292.03	B1g	386.09	B3g	681.44	Ag	841.18
B1g	48.90	B3g	75.32	B1g	118.04	B3g	195.48	B1g	294.60	B2g	388.30	Ag	682.16	B1g	843.56
Ag	49.07	B1g	75.34	B1g	120.32	B1g	197.94	B3g	302.11	Ag	390.40	B1g	687.12	Ag	845.05
B2g	49.68	B3g	76.04	Ag	124.61	B2g	199.70	B1g	303.61	B3g	396.18	B3g	691.67	B1g	849.14
B3g	51.21	Ag	77.95	B1g	126.73	Ag	200.08	Ag	306.35	Ag	397.55	B2g	695.48	B2g	849.70
B2g	51.73	B1g	78.07	Ag	132.41	B2g	202.59	B2g	306.70	B2g	405.60	B2g	702.04	B3g	853.07
B3g	52.44	B3g	80.53	B2g	132.91	B3g	205.33	B1g	311.38	B3g	406.33	Ag	702.40	B1g	858.31
B1g	52.93	B1g	80.72	B1g	133.60	Ag	207.82	B3g	312.28	B1g	407.78	B1g	704.50	B2g	862.14
Ag	53.07	B2g	81.26	B3g	136.42	B1g	208.14	Ag	312.29	B2g	412.49	B1g	741.73	B1g	864.98
B3g	53.10	B3g	81.79	Ag	137.81	B3g	208.47	Ag	315.57	B1g	414.20	Ag	744.08	B3g	870.87
B2g	55.05	B3g	83.31	B2g	139.26	B3g	208.85	B3g	316.75	Ag	414.74	B3g	746.91	Ag	875.06
B1g	55.14	B2g	83.86	Ag	140.28	Ag	210.32	B2g	318.00	B3g	417.71	B2g	750.96	B2g	875.23
Ag	55.42	B3g	84.64	B2g	141.91	B2g	210.51	B1g	320.54	B2g	418.26	Ag	754.10	B3g	883.18
B1g	56.98	Ag	84.85	B3g	141.96	B3g	211.31	B3g	328.08	Ag	421.86	B1g	757.60	B3g	890.24
B2g	59.30	B2g	85.22	B1g	144.77	Ag	217.28	B2g	330.10	B1g	423.49	B2g	759.51	B2g	901.55
B1g	59.32	B2g	86.02	Ag	145.09	B3g	218.64	B1g	330.68	B2g	425.24	B2g	773.07	B1g	902.54
Ag	59.45	B1g	86.14	B2g	148.33	B1g	219.36	Ag	333.69	Ag	426.74	Ag	776.84		
B3g	59.97	Ag	87.05	B1g	148.42	B2g	219.54	B3g	337.56	B1g	428.54	B3g	780.76		
B1g	61.18	B1g	87.16	Ag	150.36	B2g	224.10	Ag	340.02	B3g	431.29	B3g	781.62		
Ag	61.90	B3g	88.93	B3g	152.64	Ag	227.78	B2g	342.39	B2g	431.72	Ag	786.94		
B3g	62.78	B1g	89.15	Ag	152.76	B3g	232.02	B3g	343.70	B1g	433.35	B1g	791.15		
B2g	63.17	B2g	89.36	B2g	154.40	B3g	233.28	Ag	346.31	Ag	434.89	B3g	792.56		
B3g	64.14	Ag	89.89	B1g	155.54	B1g	234.76	B1g	347.65	B2g	436.40	B2g	796.09		
B1g	64.69	B2g	91.74	B3g	157.96	B2g	234.90	B3g	350.58	B1g	438.52	Ag	796.39		

Table S3: Positions of active Raman-modes (experimental and theoretical).

Types of Raman-active modes	Specific positions of the experimental Raman-active modes from Raman spectrum (cm^{-1})	Calculated theoretically positions of the Raman-active modes from optimized structure (cm^{-1})
B_{3g}		66.57
B_{2g}		67.04
A_g		67.30
B_{1g}	67	67.50
B_{2g}		67.74
B_{3g}		83.30
B_{2g}		83.86
B_{3g}		84.64
A_g	84	84.85
B_{2g}		85.22
B_{3g}		98.73
B_{2g}	100	100.03
B_{1g}		100.59
B_{2g}		165.83
A_g	166	165.99
B_{1g}		168.27
B_{1g}		243.09
A_g	243	244.58
B_{2g}		245.56
B_{2g}		261.91
B_{3g}	263	263.12
A_g		263.35
A_g	335	333.69
B_{3g}		337.56
B_{3g}	363	361.69

B_{2g}		365.35
A_g	529	508.40
B_{3g}		681.44
A_g	654	682.16
B_{1g}	672	687.12
B_{2g}	770	773.07
B_{1g}	790	791.15
B_{3g}		792.56
B_{2g}	810	809.54, 810.08
B_{1g}		827.30
B_{2g}	830	827.99
A_g		829.05
B_{3g}		833.82
B_{1g}		902.54

The structural defects associated to the electronic charge transfer processes from ordered (o) to disordered (d) clusters can be explained by the following equations (1–12):

$$[VO_4]_o^x + [VO_4]_d^x \rightarrow [VO_4]_o^{'} + [VO_4]_d^{\bullet} \quad \text{.....(1)}$$

$$[VO_5]_o^x + [VO_5]_d^x \rightarrow [VO_5]_o^{'} + [VO_5]_d^{\bullet} \quad \text{.....(2)}$$

$$[AgO_5]_o^x + [AgO_5]_d^x \rightarrow [AgO_5]_o^{'} + [AgO_5]_d^{\bullet} \quad \text{.....(3)}$$

$$[AgO_6]_o^x + [AgO_6]_d^x \rightarrow [AgO_6]_o^{'} + [AgO_6]_d^{\bullet} \quad \text{.....(4)}$$

$$[VO_4]_o^x + [VO_3.V_O^x]_d \rightarrow [VO_4]_o^{'} + [VO_3.V_O^{\bullet}]_d \quad \text{.....(5)}$$

$$[VO_4]_o^x + [VO_3.V_O^{\bullet}]_d \rightarrow [VO_4]_o^{'} + [VO_3.V_O^{\bullet\bullet}]_d \quad \text{.....(6)}$$

$$[VO_5]_o^x + [VO_4.V_O^x]_d \rightarrow [VO_5]_o^{'} + [VO_4.V_O^{\bullet}]_d \quad \text{.....(7)}$$

$$[VO_5]_o^x + [VO_4.V_O^{\bullet}]_d \rightarrow [VO_5]_o^{'} + [VO_4.V_O^{\bullet\bullet}]_d \quad \text{.....(8)}$$

$$[AgO_5]_o^x + [AgO_4.V_O^x]_d \rightarrow [AgO_5]_o^{'} + [AgO_4.V_O^{\bullet}]_d \quad \text{.....(9)}$$

$$[AgO_5]_o^x + [AgO_4.V_O^{\bullet}]_d \rightarrow [AgO_5]_o^{'} + [AgO_4.V_O^{\bullet\bullet}]_d \quad \text{.....(10)}$$

$$[AgO_6]_o^x + [AgO_5.V_O^x]_d \rightarrow [AgO_6]_o^{'} + [AgO_5.V_O^{\bullet}]_d \quad \text{.....(11)}$$

$$[AgO_6]_o^x + [AgO_5.V_O^{\bullet}]_d \rightarrow [AgO_6]_o^{'} + [AgO_5.V_O^{\bullet\bullet}]_d \quad \text{.....(12)}$$

where, $[VO_4]_d^x$, $[VO_5]_d^x$, $[AgO_6]_d^x$, $[AgO_5]_d^x$, $[VO_4.V_O^x]_d$, $[VO_5.V_O^x]_d$, $[AgO_5.V_O^x]_d$, and $[AgO_6.V_O^x]_d$ are electron donors;$[VO_4.V_O^\bullet]_d$, $[VO_5.V_O^\bullet]_d$, $[AgO_5.V_O^\bullet]_d$,and $[AgO_6.V_O^\bullet]_d$ are electron donors/acceptors; and $[VO_4]_o^x$, $[VO_5]_o^x$,$[AgO_5]_o^x$, and $[AgO_6]_o^x$ are electron acceptors.

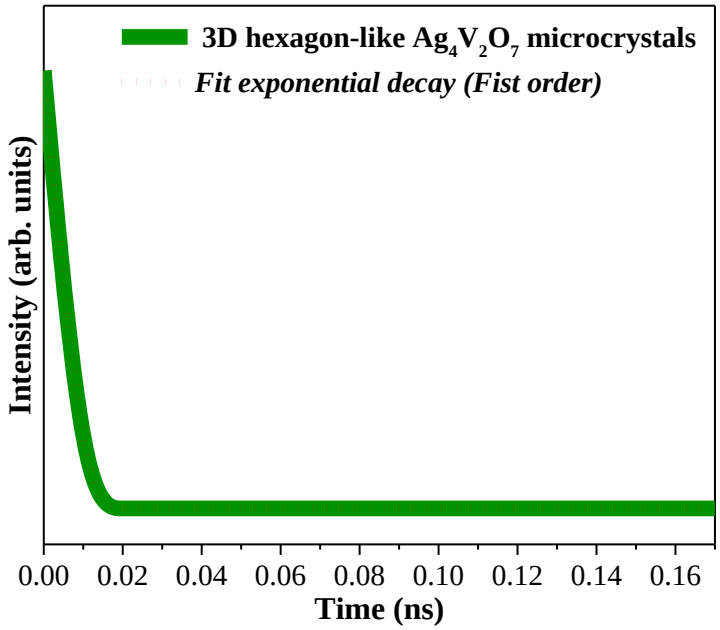

Figs. S3: Luminescence decay of 3D hexagon-like $Ag_4V_2O_7$ microcrystals [excitation wavelength (λ_{exc} = 350 nm)] monitoring the maximum PL emissions at (450 nm).

2.2. Effect of metallic Ag growth on the electrical resistance of 3D flower-like $Ag_4V_2O_7$ crystals

Abstract

In this communication, we report for the first time the nucleation and growth of metallic Ag nanoparticles on the surface of 3D flower-like $Ag_4V_2O_7$ crystals, induced by accelerated electron beam irradiation. The growth of metallic Ag on the surfaces of $Ag_4V_2O_7$ crystals were studied by transmission electron microscopy (TEM) and energy dispersive X-ray spectroscopy (EDXS). According to TEM images and EDXS analyses, exposure to the electron beam induces a reduction process and the growth of metallic Ag nanoparticles on the surface of $Ag_4V_2O_7$ crystals. Moreover, the inductively coupled plasma optical emission spectrometry measurements indicated an excess of Ag and V vacancies at $Ag_4V_2O_7$ lattice. Finally, it was observed that the electrical resistance varies considerably with the exposure time to electron beam irradiation.

1. Introduction

Due to their physical and chemical properties, silver vanadium oxide (SVO) semiconductors have a wide range of applications, including in electrochromic devices, lithium batteries, catalysts, gas sensors, and electrical and optical devices.[1-3] The literature shows that their electronic properties can be improved by incorporating metallic Ag nanoparticles (NPs) on the surface. This is because the formation of a heterojunction creates a synergistic effect between Ag NPs and SVOs, improving their electronic properties.[4]

Recently, our group discovered a unwanted real-time in situ nucleation and growth processes of metallic Ag NPs on different silver-based semiconductors, such as α-Ag_2WO_4,[5] β-Ag_2MoO_4,[6-8] Ag_3PO_4,[9] and β-$AgVO_3$.[10] The nucleation and growth processes were driven, in all cases, by accelerated electron beam irradiation from an electron microscope under high vacuum. The reasons for this physicochemical phenomenon have been discussed in recent publications.[6,8-11]

Therefore, in this communication, we present new findings on the electrical resistance changes with the growth of metallic Ag NPs in the surface of the 3D flower-like $Ag_4V_2O_7$ crystals.

2. Experimental procedure

The details related to synthesis, characterization, and setup for electrical measurements of 3D flower-like $Ag_4V_2O_7$ microcrystals are presented in Supplementary Information.

3. Results and discussion

Figure 1 shows the XRD pattern of $Ag_4V_2O_7$ crystals no irradiated by electron beams.

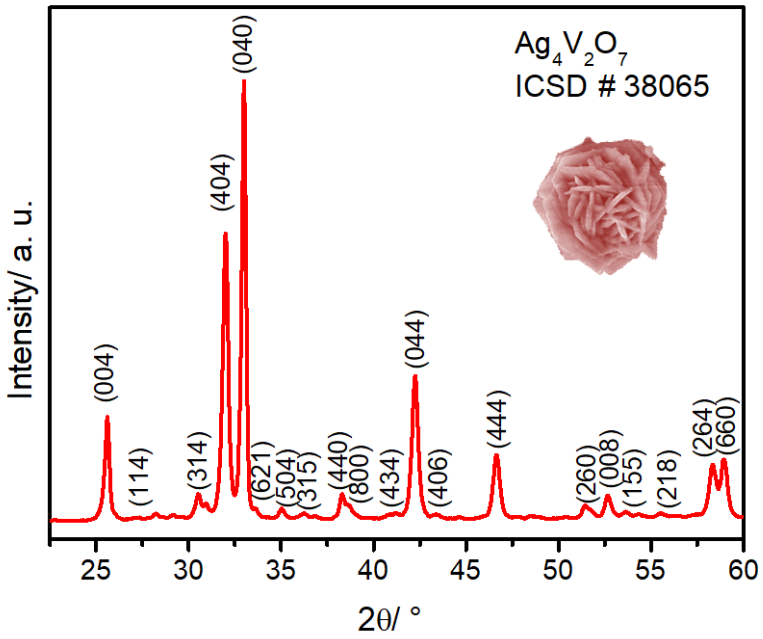

FIGURE 1 XRD patterns of 3D flowers-like $Ag_4V_2O_7$ microcrystals obtained at 0°C for 10 min.

All the diffraction peaks can be assigned to the orthorhombic structure (ICDS No. 38065, space group: Pbca).[12] The lack of other peaks demonstrates the high purity of the materials. Detailed Rietveld refinement results are displayed in Figure S1 Supplementary Information (SI). The morphology and microstructure of nonirradiated $Ag_4V_2O_7$ crystals were investigated by field-emission scanning electron microscopy (FE-SEM). In Figure 2A, can be seen that the $Ag_4V_2O_7$ crystals exhibit a uniform 3D flower and nearly spherical shape with an average diameter of 4.3 μm. The flower-like precursor is composed of very thin petals with an average thickness of approximately 170 nm.

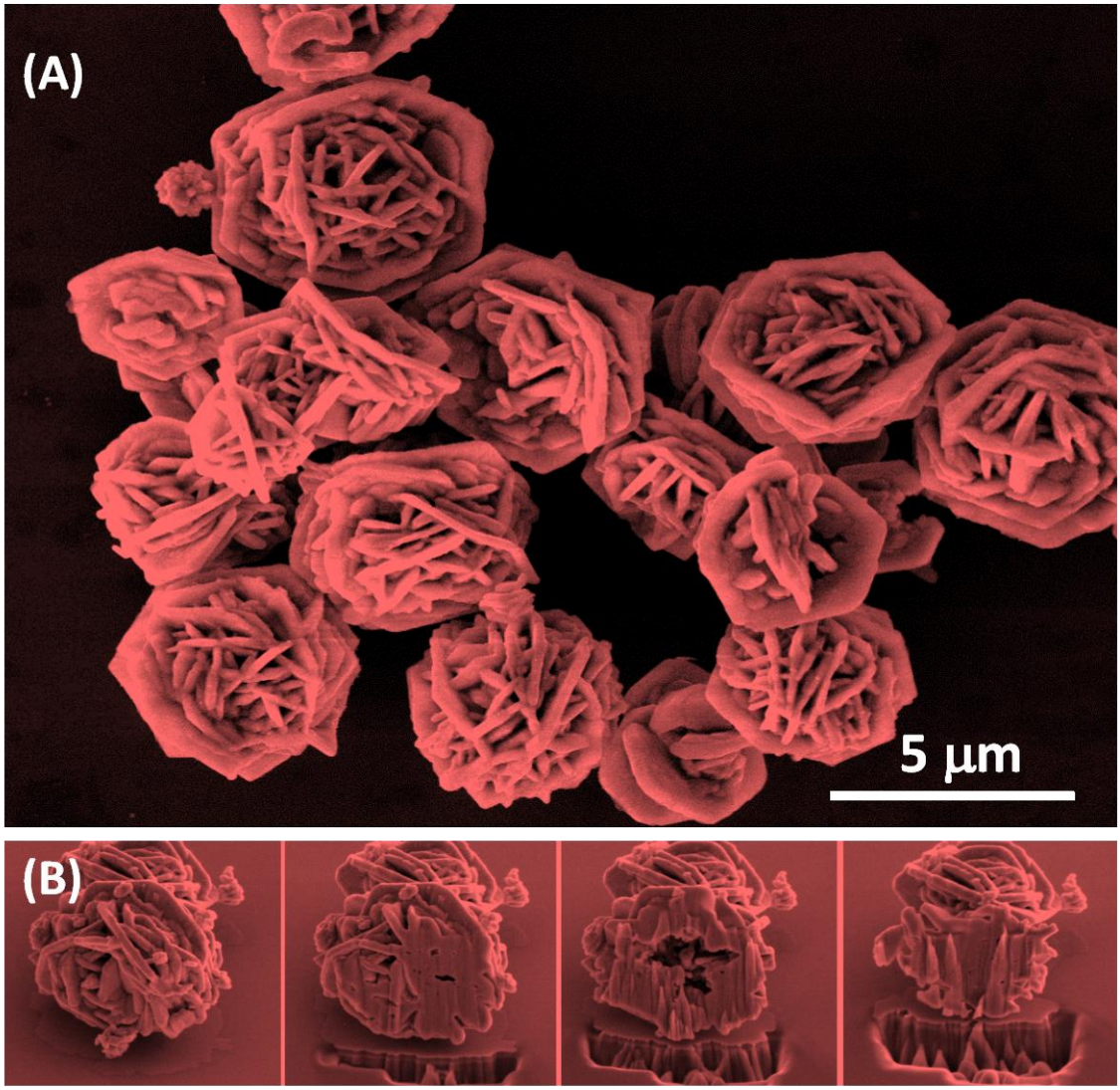

FIGURE 2 (A) Morphology and microstructure of the 3D flowers-like $Ag_4V_2O_7$ microcrystals and (B) Slicing of the 3D flowers-like $Ag_4V_2O_7$ microcrystals.

Crystal size distributions were statistically analyzed by measuring 100 microcrystals from FE-SEM images (Figure S2 in Supporting Information). Only small variations in average particle sizes were observed, confirming the monodisperse nature of these particle systems.

A possible formation mechanism of the flower-like $Ag_4V_2O_7$ crystals could be described as follows: initially vanadium and silver complex clusters form in separate aqueous solutions. When the two solutions are mixed, $Ag_4V_2O_7$ nuclei clusters form and subsequently grow. The Ostwald ripening process governs the growth mechanism. The nanocrystals pass through a self-organization process and a few tiny nanoplates (NPLs), with some poorly defined hexagonal faces develop. Ten minutes after the reaction starts, undeveloped flower-like $Ag_4V_2O_7$ crystals start forming by self-assembly and preferential

orientation process. Moreover, internal pores and channels were observed when the flower-like crystals are sliced (Figure 2B). It is believed that these defects arise from the fast nucleation process, growth, and agglomeration onset of primary NPLs at a low temperature (0°C), which lead to the formation of relatively unordered flower-like crystals.

The growth process of metallic Ag NPs on the surface of $Ag_4V_2O_7$ crystals as a function of exposure time was investigated via FE-SEM under an accelerating voltage of 10 kV. The onset of Ag nanoparticle nucleation on the surface of the $Ag_4V_2O_7$ crystals was observed (Figure 3A,B) as soon as the sample analysis by FE-SEM image was started. Figure 3A shows an SEM image of the flower-like crystals immediately after a rapid approach and focus adjustment (time zero). After 5 minute of exposure to the electron beam, the $Ag_4V_2O_7$ crystals were already showing regions with Ag NPs on the surface, as can be seen in Figure 3B.

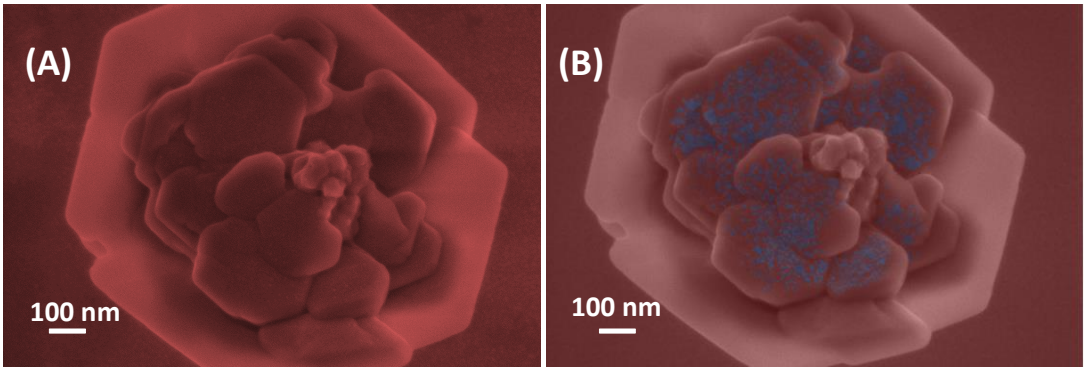

FIGURE 3 FE-SEM images of $Ag_4V_2O_7$ microcrystals: (A) before; and (B) after a 5 min exposure to the electron beam at 10 kV.

The EDXS and TEM analyses were used to prove that Ag NPs had grown on the surface of the $Ag_4V_2O_7$ crystals. The samples were subjected to electron beam irradiation in a TEM microscope for 2 minute, and two regions in the focused flower-like $Ag_4V_2O_7$ crystals were selected for examination. Figure 4A,B correspond to the sample before and after irradiation, respectively. In Figure 4B, two distinct regions (indicated in the figure by blue squares) were selected. In Region 1, Ag NPs were found and their presence was confirmed by EDXS analysis. The EDXS results (Figure 4B, Region 1) confirmed that the electron beam promoted the random growth of metallic Ag NPs. The inductively coupled plasma optical emission spectrometry (ICP-OES) measurements are presented

in Table S1 and shown in (Supporting Information) indicated an excess of Ag and V vacancies at $Ag_4V_2O_7$ lattice.

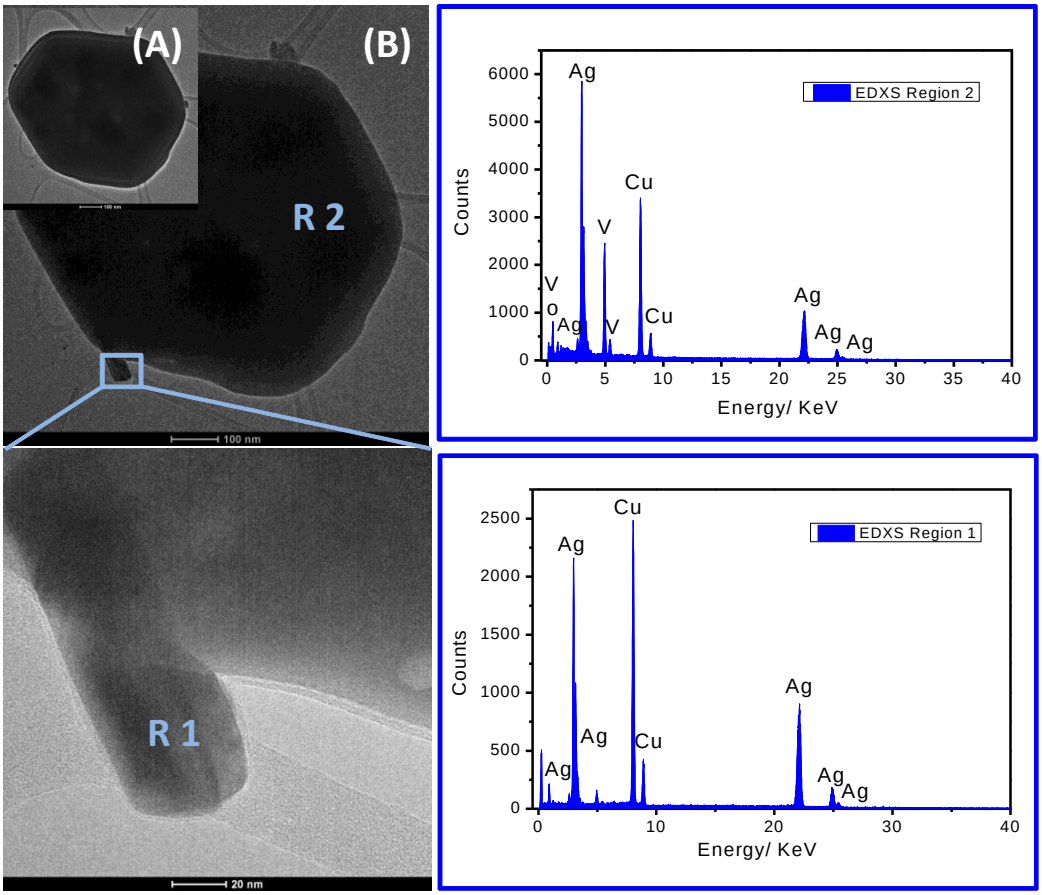

FIGURE 4 TEM images of $Ag_4V_2O_7$ microcrystals: (A) before; and (B) after a 5 min exposure to the electron beam at 10 kV.

To the best of our knowledge, this phenomenon had not been previously observed for $Ag_4V_2O_7$ and was found to occur in all regions irradiated by the electron beam. A complex clusters model based on Kröger-Vink [13] notation was employed to further explain the electrical properties of $Ag_4V_2O_7$ crystals and propose a possible electrical resistance observed at system. In this model, intrinsic (bulk/surface) defects in the lattice of the material facilitate polarization of the lattice and lead to the electronics transitions between ordered and disordered clusters. Therefore, electron (e')-hole (h•) pairs are present even before excitation of lattice. The before and after exposure to electron beam enhances the formation of e'-h• pairs leading to electron transfer within the band gap. The cluster-to-cluster charge-transfer (CCCT) in a crystal, containing more than one kind of cluster, [14] is characterized by excitations involving electronic transitions from one cluster to another, which is possible according to Equations (1-6):

$$\xrightarrow{e\prime} [Ag_4V_2O_7]_{(defects)} \rightarrow 4Ag_i + 2V_V^{2\prime} + 7O_o^x \text{.....(1)}$$

$$\xrightarrow{e\prime} [Ag_4V_2O_7]_{(defects)} \rightarrow [AgO_6]_o^x - [AgO_6]_d^x + [AgO_5]_o^x - [AgO_5]_d^x + [VO_5]_o^x - [VO_5]_d^x + [VO_4]_o^x - [VO_4]_d^x \text{.....(2)}$$

$$[AgO_6]_o^x - [AgO_6]_d^x \xrightarrow{e\prime} [AgO_6]_o^{\prime} - [AgO_6]_d^{\bullet} \text{.....(3)}$$

$$[AgO_5]_o^x - [AgO_6]_d^x \xrightarrow{e\prime} [AgO_6]_o^{\prime} + [AgO_6]_d^{\bullet} \text{.....(4)}$$

$$[VO_5]_o^x - [VO_5]_d^x \xrightarrow{e\prime} [VO_5]_o^{\prime} - [VO_5]_o^{\bullet} \text{.....(5)}$$

$$[VO_4]_o^x - [VO_5]_d^x \xrightarrow{e\prime} [VO_4]_o^{\prime} - [VO_4]_o^{\bullet} \text{.....(6)}$$

When the surface of 3D flower-like $Ag_4V_2O_7$ crystals is irradiated with an electron beam, the lattice composed by ordered(o)/disordered(d) $[AgO_5]$/$[AgO_5]$ and o/d $[VO_5]$/ $[VO_4]$ clusters interact with the incoming electrons, resulting in the reduction process of Ag NPs, formation of excess Ag and interstitial Ag (Ag_i), as well as the formation of *V* vacancies ($V_V^{2\prime}$). Moreover, Ag migrates from the bulk to the surface; hence, regions in the crystal lattice with negatively charged vacancies form. This process induces a short- and medium-range disorder within the material. The regions where the metallic Ag has migrated exhibit a *p*-type semiconducting behavior. Since $Ag_4V_2O_7$ crystal is an *n*-type semiconductor and oxygen vacancies ($V_O^{\bullet}$) are already present, an *n/p* interface is created between the Ag NPs and $Ag_4V_2O_7$ crystals, thereby forming a semiconductor diode. A semiconductor diode has the valuable property that electrons only flow in one direction across it, and as a result, it acts as a rectifier.[10]

Since the Ag growth on flower-like $Ag_4V_2O_7$ crystals can affect the electrical properties of the material, electrical resistance measurements were performed, and the results were evaluated as a function of the exposure time, ie, as a function of the growth of these metallic Ag nanoparticles. Figure 5 shows the variation in the electrical resistance

of flower-like $Ag_4V_2O_7$ crystals subjected to electron beam irradiation at different exposure times.

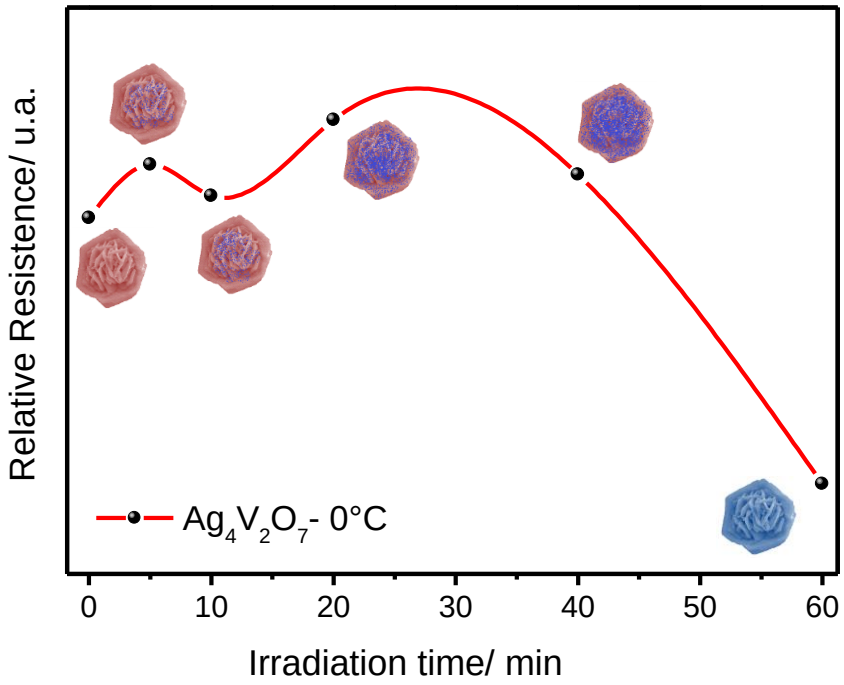

FIGURE 5 Variation in the electric resistance of $Ag_4V_2O_7$ microcrystals subjected to electron beam irradiation for different times.

Before the formation of Ag NPs, the electrical resistance is governed by the bulk properties, the shape of the crystals, and the presence of pores and channels in the bulk. After 5 minute irradiation, a slight increase in resistance is observed, which can be attributed to the pores and channels in the bulk. From this time until 10 minute, the bulk and surface properties equally contribute to the semiconductor resistance. After 10 minute, the growth of Ag NPs silver on the $Ag_4V_2O_7$ surface creates Ag vacancies (V'_{Ag}), Ag_i and $V_V^{2\prime}$ in the semiconductor bulk (Equation 1). The formation of negative V'_{Ag}, along with the already present oxygen vacancies ($V_O^{\bullet}$), causes an increase in the electrical resistance of the semiconductor, until the irradiation time reaches 27 minute. However, after 27 minute, the resistance decreases, probably due to the formation of a thick layer of metallic Ag on the $Ag_4V_2O_7$ semiconductor surface, which continues to grow with the irradiation time. Since the Ag is the best-known electric conductor (room temperature), this growth of the Ag metallic layer acts decreasing the electrical resistance of the material.

4. Conclusion

In summary, we have observed, for the first time, that electron beam irradiation, such as that produced by FE-SEM/TEM, induces the formation and growth of metallic Ag NPs on the surface of 3D flower-like $Ag_4V_2O_7$ crystals. ICP-OES measurements showed the presence of V vacancies and excess of Ag at $Ag_4V_2O_7$ lattice. Moreover, it was observed that the electrical resistance of the flower-like Ag4V2O7 crystals is largely influenced by the growth of Ag NPs on the surface of the semiconductor. Therefore, the irradiation generated Ag NPs have two advantageous effects: the formation of Ag NPs on the crystal surface and control of the semiconductor properties by electron beam irradiation.

Acknowledgments

The authors acknowledge the financial support of agencies: CAPES (PNPD – 1268069), FAPESP (2013/07296-2; 2013/26671- 9), and CNPq (304531/2013-8).

References

1. Ran R, McEvoy JG, Zhang Z. $Ag_2O/Ag_3VO_4/Ag_4V_2O_7$ heterogeneous photocatalyst prepared by a facile hydrothermal synthesis with enhanced photocatalytic performance under visible light irradiation. Mater Res Bull. 2016;74:140-150.
2. Zeng H, Wang Q, Rao Y. Ultrafine β-$AgVO_3$ nanoribbons derived from α-$AgVO_3$ nanorods by water evaporation method and its application for lithium ion batteries. RSC Adv. 2015;5:3011-3015.
3. Sharma S, Panthöfer M, Jansen M, Ramanan A. Ion exchange synthesis of silver vanadates from organically templated layered vanadates. Mater Chem Phys. 2005;91:257-260.
4. Zhao W, Guo Y, Faiz Y, et al. Facile in-suit synthesis of $Ag/AgVO_3$ one-dimensional hybrid nanoribbons with enhanced performance of plasmonic visible-light photocatalysis. Appl Catal B: Environm. 2015;163:288-297.
5. Longo E, Cavalcante LS, Volanti DP, et al. Direct in situ observation of the electron-driven synthesis of Ag filaments on α-Ag_2WO_4 crystals. Sci Rep. 2013;3:1676-1680.
6. Alvarez Roca R, Lemos PS, Andrés J, Longo E. Formation of Ag nanoparticles on metastable β-Ag_2WO_4 microcrystals induced by electron irradiation. Chem Phys Lett. 2016;644:68-72.
7. De Santana YVB, Gomes JEC, Matos L, et al. Silver molybdate and silver tungstate nanocomposites with enhanced photoluminescence. Nanomater Nanotechnol. 2014;4:22-31.

8. Andrés J, Ferrer MM, Gracia L, et al. A combined experimental and theoretical study on the formation of Ag filaments on β-Ag_2MoO_4 induced by electron irradiation. Part Part Syst Char. 2015;32:646-651.

9. Botelho G, Sczancoski JC, Andres J, Gracia L, Longo E. Experimental and theoretical study on the structure, optical properties, and growth of metallic silver nanostructures in Ag_3PO_4. J Phys Chem C. 2015;119:6293-6306.

10. Oliveira RC, Assis M, Teixeira MM, et al. An experimental and computational study of β-$AgVO_3$: optical properties and formation of Ag nanoparticles. J Phys Chem C. 2016;120:12254- 12264.

11. Fabbro MT, Gracia L, Silva GS, et al. Understanding the formation and growth of Ag nanoparticles on silver chromate induced by electron irradiation in electron microscope: a combined experimental and theoretical study. J Solid State Chem. 2016;239:220- 227.

12. Masse R, Averbuch-Pouchot MT, Durif A, Guitel JC. Chemical preparation and crystal structure of silver pyrovanadate, $Ag_4V_2O_7$. Act Cryst. 1983;C39:1608-1610.

13. Kröger FA, Vink HJ. Relations Between the Concentrations of Imperfections in Crystalline Solids. Solid State Phys. 3rd edn. Amsterdam, the Netherland: Elsevier; 1956.

14. Oliveira RC, Gracia L, Assis M, et al. Disclosing the electronic structure and optical properties of $Ag_4V_2O_7$ crystals: experimental and theoretical insights. Cryst Eng Comm. 2016;18:6483- 6491.

Supplementary Information

Effect of metallic Ag growth on the electrical resistance of 3D flower-like $Ag_4V_2O_7$ crystals

R.C. de Oliveira[a], S.M. Zanetti[b], M. Assis[a], M. Penha[a], M. Mondego[a], M. Cilense[b], E. Longo[b], L.S. Cavalcante[c*]

[a] INCTMN-CDMF, Universidade Federal de São Carlos, P.O. Box 676, 13565-905 São Carlos, SP, Brazil

[b]INCTMN-UNESP, Universidade Estadual Paulista, P.O. Box 355, 14801-907 Araraquara, SP, Brazil

[c] PPGQ-DQ, Universidade Estadual do Piauí, Rua: João Cabral, N. 2231, P.O. Box 381, 64002-150, Teresina–PI, Brazil

2.1. Synthesis of 3D flower-like $Ag_4V_2O_7$ microcrystals

The 3D flower-like $Ag_4V_2O_7$ microcrystals were obtained by controlled precipitation method at 0 ºC for 10 min. The precursors utilized in this synthesis were silver nitrate, $AgNO_3$ (99% purity, Synth) and ammonium monovanadate, NH_4VO_3 (99% purity, Aldrich). Initially, 1mmol de NH_4VO_3 was dissolved in 60 mL distilled water at 30°C, under magnetic stirring for 15 min. Then, 1mmol of $AgNO_3$ was dissolved in 15 mL distilled water, under magnetic stirring for 15 min, to this solution a few drops of ammonium hydroxide (NH_4OH) (30% in NH_3, Synth) was added until the solution becomes clear. Both solutions were placed in an ice bath at 0 ºC and quickly mixed promoting the instantaneous formation $Ag_4V_2O_7$ precipitate (orange coloration). The precipitated was settled at 0 ºC during 10 min, followed by centrifugation, washing with distilled water several times, and drying in a conventional furnace at 60ºC for 10 hours.

2.2. Characterization

The $Ag_4V_2O_7$ crystals were characterized by XRD using $Cu_{K\alpha}$ radiation (λ = 1.5406 Å) (Rigaku diffractometer, Model D/Max-2500PC, Japan) in the 2θ range of 10 to 80° at a scan speed of rate of 2°/min and from 10 to 110° with at a scan speed of 1°/min in the Rietveld routine, both with a step of 0.02°. The morphology was investigated with a field emission scanning electron microscope (FE-SEM) Supra 35-VP Carl Zeiss (Germany) operating at 15 kV. The crystals were sliced in a focused ion beam (FIB) microscope (FEI, Helios NanoLab 600i) to observe the intracrystal microstructure. In addition, TEM, at 200 kV and EDS measurements were performed using a FEI microscope (model Tecnai G2 F20, USA). The inductively coupled plasma optical emission spectrometry (ICP-OES) measurements were carried out using an iCAP 6500 duo ICP OES (Thermo Scientific, USA) and the operating conditions are described in Table 1. The standard solutions of Ag and V were prepared by adequate dilution of single-element (1000 mg L^{-1}) stock solutions (Fluka Analytical, St. Gallen, Switzerland) in 1% (v/v) HNO_3. The $Ag_4V_2O_7$ sample was solubilized in a solution composed by 495 mL of H_2O_2 (Synth, P.A, 29%) and 5 mL of HNO_3 (Synth, P.A. 65%).

Table S1: Operational conditions for the iCAP 6500 duo ICP-OES.

Parameter	Operating condition
RF Power (W)	1150
Auxiliary gas fow rate (L min $^{-1}$)	0.5
Plasma gas fow rate (L min $^{-1}$)	12.0
Nebulizer gas fow rate (L min $^{-1}$)	0.7
Pump speed (rpm)	50
Stabilization time (s)	5
Integration time (s)	15
Replicates	3
Viewing mode	Axial
Wavelengths (nm)	338,2 (Ag) and 292,4 (V)

Initially, 0.01384 g of $Ag_4V_2O_7$ was solubilized in 500 mL of hydrogen peroxide solution with 10% nitric acid. Therefore, theoretically, the V concentration was 4.3698×10^{-3} g.L^{-1} (4.2890×10^{-5} mols) and Ag (8.5781×10^{-5} mols) 18.5064×10^{-3} g.L^{-1}. This solution was added in a tube containing 15 mL H_2O, so the final concentration of V is 1.09246×10^{-3} g.L^{-1} and Ag is 4.6266×10^{-3} gL^{-1}. According to the experimental result of ICP-OES measurements, the concentration of V in solution is 0.9291×10^{-3} g.L^{-1} and Ag is 4.42×10^{-3} g.L^{-1}. Which corresponds to $3.64728\text{x}10^{-5}$ mols of V and 8.1950×10^{-5} mols Ag in solution. The conclusion we have is that, there is an excess of Ag (or vacancies of V), since for 3.64728×10^{-5} mols of V it was expected to obtain 7.299456×10^{-5} mols of Ag (excess of 0.9×10^{-5} mols of Ag).

2.3. *Set-up for electrical measurements*

A thick film of $Ag_4V_2O_7$ nanoparticles covering the gap between the two ITO pieces was obtained. A nonconducting gap was obtained in an indium tin oxide (ITO) glass by scratching the conductive surface separating into two pieces, thus each piece was adopted as an electrode. The as-synthesized $Ag_4V_2O_7$ nanoparticles were turned into a paste by mixing with isopropanol which was poured on the surface of the gap between the two electrodes. The set-up was dried overnight at 70 ^{o}C and kept in a low humidity environment obtained by silica-gel until be exposed to electron beam for irradiation for different times in a scanning electron microscope (SEM, Topcon, SM300).

The I x V (Keithley 2400 Source Meter) measurements were carried out at room temperature on the thick film before and after exposure to electron beam at 30 kV for 5, 10, 20, 40 and 60 min. To avoid the influence of the external environment, all measurements were done in a closed cell filled with silica gel to keep a low humidity level. The electrical resistance was calculated through the slope of the I x V curve.

3. Results and Discussions

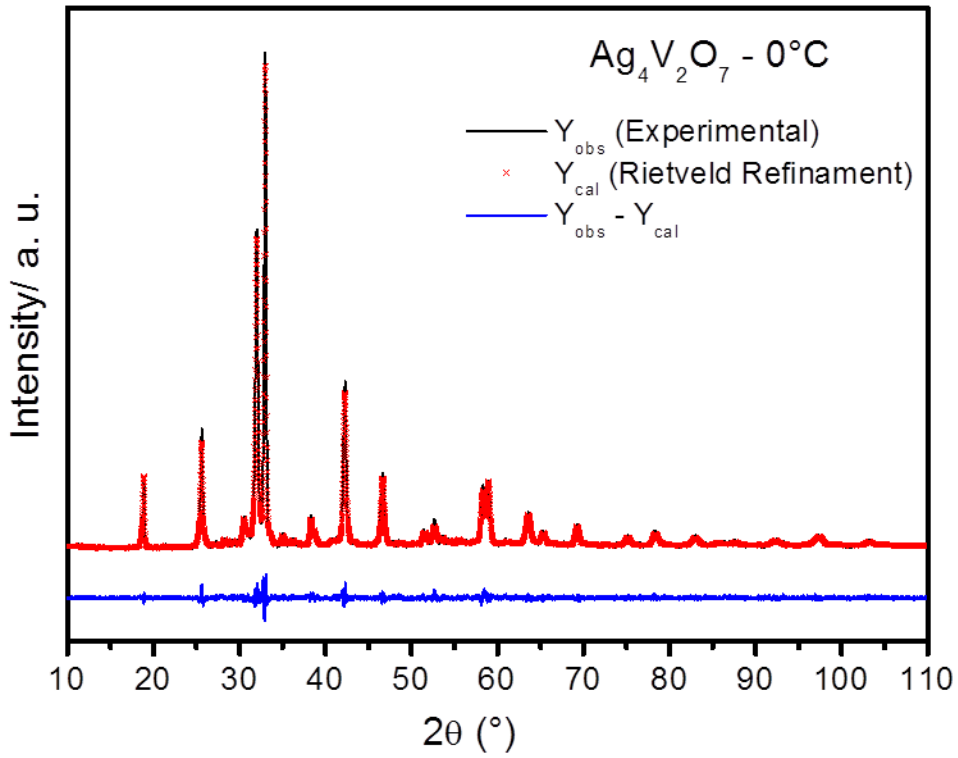

Figure S1: Rietveld refinement plot of 3D flower-like $Ag_4V_2O_7$ microcrystals obtained by controlled precipitation method at 0 ºC for 10 min.

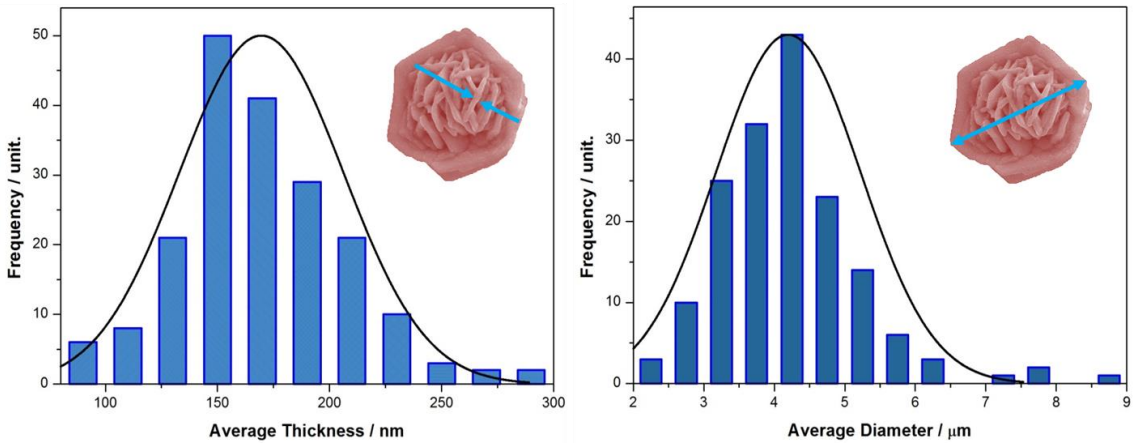

Figure S2: Analyses of the size distribution by measuring 100 microcrystals from FE-SEM images.

3. GENERAL CONCLUSION

In summary, in this study, $Ag_4V_2O_7$ powders pure, with controlled morphologies were obtained by the CP method. By the combination of experimental techniques and first-principles DFT calculations, new information about the geometry, cluster coordination, and electronic structure of $Ag_4V_2O_7$ microcrystals was presented. Besides that, for the first time, we report the nucleation and growth of metallic Ag NPS on the surface of 3D flower-like $Ag_4V_2O_7$, induced by accelerated electron beam irradiation. The growth of metallic Ag on the surfaces of $Ag_4V_2O_7$ crystals were studied by TEM and EDXS. According to TEM images and EDXS analyses, exposure to the electron beam induces a reduction process and the growth of metallic Ag nanoparticles on the surface of $Ag_4V_2O_7$ crystals. Finally, it was observed that the electrical resistance varies considerably with the exposure time to electron beam irradiation.

4. REFERENCES

Alvarez Roca, R., P. S. Lemos, J. Andrés and E. Longo (2016). "Formation of Ag nanoparticles on metastable β-Ag2WO4 microcrystals induced by electron irradiation." Chemical Physics Letters **644**: 68-72.

Botelho, G., J. C. Sczancoski, J. Andres, L. Gracia and E. Longo (2015). "Experimental and Theoretical Study on the Structure, Optical Properties, and Growth of Metallic Silver Nanostructures in Ag3PO4." The Journal of Physical Chemistry C **119**(11): 6293-6306.

Dai, X. J., Y. S. Luo, W. D. Zhang and S. Y. Fu (2010). "Facile hydrothermal synthesis and photocatalytic activity of bismuth tungstate hierarchical hollow spheres with an ultrahigh surface area." Dalton Trans **39**(14): 3426-3432.

Fabbro, M. T., L. Gracia, G. S. Silva, L. P. S. Santos, J. Andrés, E. Cordoncillo and E. Longo (2016). "Understanding the formation and growth of Ag nanoparticles on silver chromate induced by electron irradiation in electron microscope: A combined experimental and theoretical study." Journal of Solid State Chemistry **239**: 220-227.

Fabbro, M. T., C. Saliby, L. R. Rios, F. A. La Porta, L. Gracia, M. S. Li, J. Andrés, L. P. S. Santos and E. Longo (2016). "Identifying and rationalizing the morphological, structural, and optical properties of -

Ag2MoO4microcrystals, and the formation process of Ag nanoparticles on their surfaces: combining experimental data and first-principles calculations." Science and Technology of Advanced Materials **16**(6): 065002.
Geoffrey A Ozin, A. A., Ludovico Cademartiri (2008). Nanochemistry : a chemical approach to nanomaterials. Great Britain, UK: Royal Society of Chemistry.
Ju, P., H. Fan, B. Zhang, K. Shang, T. Liu, S. Ai and D. Zhang (2013). "Enhanced photocatalytic activity of β-AgVO3 nanowires loaded with Ag nanoparticles under visible light irradiation." Separation and Purification Technology **109**: 107-110.
Kakihana, M. (1996). "“Sol-Gel” Preparation of High Temperature Superconducting Oxides." Journal of Sol-Gel Science and Technology **6**: 7.
Lin, C., C. Jiexin, W. Cong, C. Pig, P. De'an and A. A. Volink (2012). "Anti-tumor activity of self-charged (Eu,Ca):WO3 and Eu:CaWO4

nanoparticles." Bulletin Materials Science **35**(5): 767.
Linic, S., P. Christopher and D. B. Ingram (2011). "Plasmonic-metal nanostructures for efficient conversion of solar to chemical energy." Nat Mater **10**(12): 911-921.
Longo, E., W. Avansi, Jr., J. Bettini, J. Andres and L. Gracia (2016). "In situ Transmission Electron Microscopy observation of Ag nanocrystal evolution by surfactant free electron-driven synthesis." Sci Rep **6**: 21498.
Longo, E., L. S. Cavalcante, D. P. Volanti, A. F. Gouveia, V. M. Longo, J. A. Varela, M. O. Orlandi and J. Andres (2013). "Direct in situ observation of the electron-driven synthesis of Ag filaments on alpha-Ag2WO4 crystals." Sci Rep **3**: 1676.
Longo, V. M., C. C. De Foggi, M. M. Ferrer, A. F. Gouveia, R. S. Andre, W. Avansi, C. E. Vergani, A. L. Machado, J. Andres, L. S. Cavalcante, A. C. Hernandes and E. Longo (2014). "Potentiated electron transference in alpha-Ag2WO4 microcrystals with Ag nanofilaments as microbial agent." J Phys Chem A **118**(31): 5769-5778.
Luo, Y., X. Liu, X. Tang, Y. Luo, Q. Zeng, X. Deng, S. Ding and Y. Sun (2014). "Gold nanoparticles embedded in Ta2O5/Ta3N5as active visible-light plasmonic photocatalysts for solar hydrogen evolution." Journal of Materials Chemistry A **2**(36): 14927.
Moreira, M. L., G. P. Mambrini, D. P. Volanti, E. R. Leite, M. O. Orlandi, P. S. Pizani, V. R. Mastelaro, C. O. Paiva-Santos, E. Longo and J. A. Varela (2008). "Hydrothermal Microwave: A New Route to Obtain Photoluminescent Crystalline BaTiO3 Nanoparticles." Chemistry of Materials **20**(16): 5381-5387.
Muthamizh, S., R. Suresh, K. Giribabu, R. Manigandan, S. Praveen Kumar, S. Munusamy and V. Narayanan (2015). "MnWO4 nanocapsules: Synthesis, characterization and its electrochemical sensing property." Journal of Alloys and Compounds **619**: 601-609.
Oliveira, R. C., M. Assis, M. M. Teixeira, M. D. P. da Silva, M. S. Li, J. Andres, L. Gracia and E. Longo (2016). "An Experimental and Computational Study of β-$AgVO_3$: Optical Properties and Formation of Ag Nanoparticles." The Journal of Physical Chemistry C **120**(22): 12254-12264.
Oliveira, R. C. d., L. Gracia, M. Assis, M. S. Li, J. Andres, E. Longo and L. S. Cavalcante (2016). "Disclosing the Electronic Structure and Optical Properties of

Ag4V2O7 crystals: Experimental and Theoretical Insights." Crystal Engineering Communication.
Rajagopal, S., D. Nataraj, O. Y. Khyzhun, Y. Djaoued, J. Robichaud and D. Mangalaraj (2010). "Hydrothermal synthesis and electronic properties of FeWO4 and CoWO4 nanostructures." Journal of Alloys and Compounds **493**(1-2): 340-345.
S., P., J. Andres, L. Gracia, M. A. San-Miguel, E. Z. da Silva, E. Longo and V. M. Longo (2015). "Elucidating the real-time Ag nanoparticle growth on alpha-Ag2WO4 during electron beam irradiation: experimental evidence and theoretical insights." Phys Chem Chem Phys **17**(7): 5352-5359.
Segal, D. (1997). "Chemical synthesis of ceramic materials." Journal of Materials Chemistry **7**(8): 1297-1305.
Sellami, N., A. Melliti, A. Sahli, M. A. Maaref, C. Testelin and R. Kuszelewiez (2009). "The effect of the excitation and of the temperature on the photoluminescence circular polarization of AlInAs/AlGaAs quantum dots." Applied Surface Science **256**(5): 1409-1412.

Silva, R. F. Goncalves, I. C. Nogueira, V. M. Longo, L. Mondoni, M. G. Moron, Y. V. Santana and E. Longo (2016). "Microwave-assisted hydrothermal synthesis of Ag(2)(W(1-x)Mox)O(4) heterostructures: Nucleation of Ag, morphology, and photoluminescence properties." Spectrochim Acta A Mol Biomol Spectrosc **153**: 428-435.

Xu, D., B. Cheng, J. Zhang, W. Wang, J. Yu and W. Ho (2015). "Photocatalytic activity of Ag2MO4(M = Cr, Mo, W) photocatalysts." J. Mater. Chem. A **3**(40): 20153-20166.

Yu, C., L. Wei, X. Li, J. Chen, Q. Fan and J. C. Yu (2013). "Synthesis and characterization of Ag/TiO2-B nanosquares with high photocatalytic activity under visible light irradiation." Materials Science and Engineering: B **178**(6): 344-348.